Anoxic Iron Sulfides Formation

A Novel Approach for Iron Removal in Groundwater Treatment

Tjark Holst

TU Delft

Anoxic Iron Sulfides Formation

A Novel Approach for Iron Removal in Groundwater Treatment

By

Tjark Holst

In partial fulfilment of the requirements for the degree of

Master of Science

in Civil Engineering

at the Delft University of Technology

to be defended publicly on Friday May 26, 2023 at 9:00 AM.

The cover picture displays a pyrite seeding crystal from the experiments, showcasing iridescence caused by intense lighting and rough texture of deposits. Golden areas have been gently wiped off. The back cover shows the same crystal under less intense lighting conditions.

Supervisor:	Ir. Roos Goedhart	(TU Delft - CEG)
	Prof. Dr. Ir. Doris van Halem	(TU Delft - CEG)
	Prof. Dr. Ir. Mark van Loosdrecht	(TU Delft - AS)

TU Delft

ACKNOWLEDGEMENTS

I would like to express my deepest gratitude to Prof. Dr. Ir. Doris van Halem for proposing this interesting topic and supervising me. Especially the various perspectives to look at my data clearly inspired me. Discussing my approaches and results with you always increased my curiosity and motivation.

I am extremely grateful to Prof. Dr. Ir. Mark van Loosdrecht for providing invaluable recommendations for my research design and supervising me. You have given me interesting perspectives on how to conduct my experiments and interpret my results.

I could have not undertaken this journey without Roos Goedhart. Thank you for your supervision throughout my thesis. I really enjoyed working together with you. You inspired me not only professionally but also food wise by recommending nice vegan recipes and restaurants.

Special thanks also to Nienke Koudijs for introducing me to the EBT laboratories, discussing approaches and fixing glovebox issues together. I would like to extend my sincere thanks to the lab technicians at EBT and the Water Lab.

I am also grateful for all the friends I have made during my master's studies at TU Delft. Especially, my housemates which gave me a warm welcome in the Netherlands, when COVID still determined our lives and online education was the norm.

Des Weiteren bin ich meiner Familie sehr dankbar. Bei euch weiß ich, dass ich immer ein offenes Ohr finde und Unterstützung bekomme!

Und nicht zuletzt, natürlich vielen Dank an Clara für deine Unterstützung. Ich bin froh dich an meiner Seite zu haben!

ABSTRACT

Groundwater (GW) makes up roughly half of the global drinking water supply. Conventional iron removal in GW treatment produces approximately 10,000t/d of iron sludge. Iron sludge consists of low-density flocs with low to no commercial value and causes frequent energy intensive backwashing of the rapid sand filter. This study aims to explore the novel concept of iron removal via iron sulfides formation. Iron sulfides are usually forming dense structures and offer a wider range of re-use applications.

To investigate this, an up-flow column reactor filled with pyrite seeding crystals was built and fed with iron and sulfide containing solutions. Flushed out formed solids were investigated with X-ray diffraction analysis and Raman spectroscopy. Seeding crystals were analyzed with scanning electron microscopy with energy dispersive X-ray spectroscopy.

This study observed rapid mackinawite formation after a few minutes. Mackinawite was likely retained by electrostatic adhesion on the pyrite seeding crystals. The molar ratio of removed iron to removed sulfide equaled up to 0.8 ± 0.2 mol Fe_{rem}/(mol S^{2-}_{rem}).

Mackinawite formation can present an interesting alternative to conventional iron removal, due to (i) its compact size, (ii) fast formation rates and (iii) possibly simple removal mechanism via electrostatic adhesion. Furthermore, in-situ formed mackinawite has the potential to simultaneously treat a wide range of pollutants ranging from toxic metals and metalloids such as arsenic over organic contaminants and nutrients such as nitrate and phosphate. Moreover, in-situ electrochemical dosing of sulfide by sulfate reduction might present a chemical-free solution for this approach. These potential synergies should be addressed in further investigations.

TABLE OF CONTENTS

List of Abbreviations

Abbreviation	Explanation
BET	Brunauer, Emmett and Teller Theory
DI	Deionized (Water)
DW	Drinking Water
EC	Electrical Conductivity
Fe_{rem}:S^{2-}_{rem}	Molar Ratio of Removed Iron to Removed Sulfide
$FeS_{2,ma}$	Marcasite
$FeS_{2,p}$	Pyrite
FeS_m	Mackinawite
GW	Groundwater
HRT	Hydraulic Retention Time
PDI	Potential-Determining Ions
PZC	Point of Zero Charge
RSF	Rapid Sand Filtration
SEM-EDX	Scanning Electron Microscopy with Energy Dispersive X-ray Spectroscopy
SI	Saturation Index
T	Temperature
XRD	X-Ray Diffraction Analysis

List of Figures

List of Tables

1 Introduction

Groundwater (GW) is one of the major sources for drinking water (DW) production worldwide, making up roughly half of the global DW supply [1]. One widely present groundwater constituent is dissolved iron(II), which is conventionally removed via aeration followed by rapid sand filtration (RSF). It is estimated that improving the iron removal method is a major factor for improving the sustainability of GW treatment [2]–[4]. Therefore, the aim of this thesis was to explore anoxic iron removal via iron sulfides formation as novel concept for GW treatment.

This chapter starts with background information on conventional iron removal in groundwater treatment (1.1). Section 1.2 introduces the research problem and states the motivation for iron removal via anoxic iron sulfides formation. The research questions and objectives are presented in section 1.3. Lastly, an outline of the thesis is given (1.4).

1.1 Background: Conventional Iron Removal in Groundwater Treatment

Groundwater is one of the major sources for drinking water supply worldwide. For instance, in Europe groundwater serves for ca. 75% of the overall drinking water demand [1]. The main reasons for this are the accessibility and the usually relatively high raw water quality, which requires only minor treatment efforts to reach drinking water standards.

However, typical constituents which need removal are iron, manganese, calcium, magnesium, and carbon dioxide. In areas with higher organic loads ammonium, methane and hydrogen sulfide supplement this list [5]–[7]. Anthropogenic influences can further lead to the presence of pharmaceutical residuals and pesticides [8].

A commonly found simple groundwater treatment scheme is shown in Figure 1-1. It consists of two treatment steps: Aeration cascades and RSF. The cascades aerate the water and strip CO_2 and possibly occurring H_2S and CH_4. The RSF removes suspended solids (e.g. iron flocs and sand), pathogenic microorganisms (90-99%), manganese and ammonium [9].

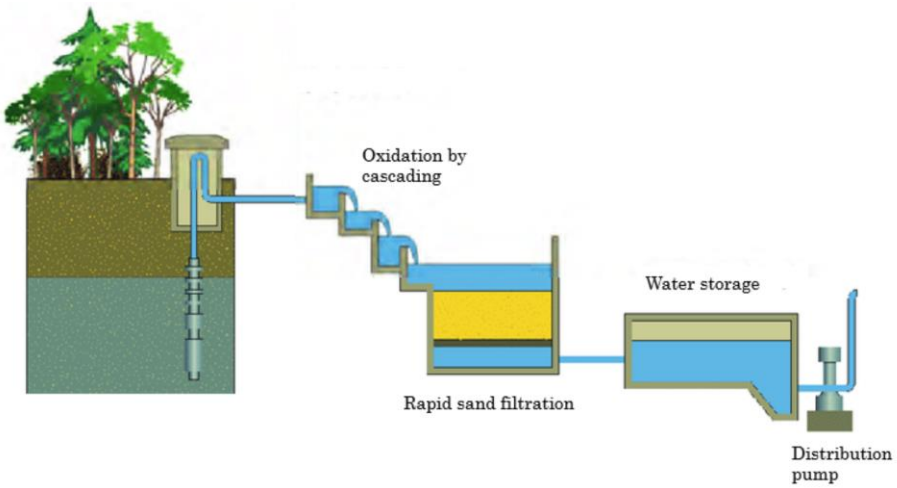

Figure 1-1 Typical GW treatment scheme. From left to right: Abstraction well, cascades, RSF, storage reservoir and distribution pump. Figure from [10] modified by [11].

This research focuses on the removal of iron. The main reasons for iron removal are to prevent discolorations, a metallic taste, and to keep the distribution network from clogging. Iron concentrations in groundwater can range from 0 to >50 mg/L [12]. The limit set by the World Health Organization for drinking water is 0.3mg/L [13].

Iron removal mechanisms can be classified into four categories : conventional, biological, membrane technology-based and nanotechnology-based strategies [14]. In GW treatment conventionally the method of “oxidation-precipitation-filtration” is utilized, where iron(II) is oxidized to iron(III), which then precipitates as $Fe(OH)_3$ and is subsequently retained by the RSF. This is illustrated by equation (1) [9].

$$4\,Fe^{2+} + O_2 + 2\,H_2O + 8\,HCO_3^- \rightarrow 4\,Fe(OH)_3 + 8\,CO_2 \quad (1)$$

The conventional method produces vast amounts of iron sludge leading to frequent energy intensive backwashing of the RSF. It is estimated that 10,000t/d of iron sludge are produced on a global scale [15]. Iron sludge is up until now of little to no commercial value with only a few applications e.g. to control sulfide in sewer systems [16] and biogas applications [17].

This leads to the concept of dosing an anion which can react to form a dense crystal and/or lead to a product of higher value compared to the bulky non valuable iron sludge. A previous study investigated this mechanism forming vivianite [18] for the removal of iron from GW by dosing PO_4^{3-}. Furthermore, indicative batch tests looked into the precipitate volume produced by SO_4^{2-}, and CO_3^{2-} addition [11]. However, the volume of precipitates formed by SO_4^{2-} and CO_3^{2-} addition appeared to be too high to present an alternative to conventional treatment and PO_4^{3-} is a valuable compound on its own [19]. This leads to the concept of dosing sulfide (S^{2-}) which is known to readily react with iron to from a wide range of compact iron sulfides [20]. One commonly found iron sulfide is pyrite (Fool’s Gold, $FeS_{2,p}$), a dense crystal often formed in anoxic sediments [21].

Numerous iron sulfides formation experiments have investigated formation mechanisms at ambient temperatures in aqueous solutions and formation rates and conditions are established [21]. Experimental investigations on the formation of iron sulfides, such as pyrite, typically aimed to achieve the following objectives: (i) understand the fundamental formation pathways, (ii) grasp the formation processes in natural systems like marine sediments, and (iii) produce pyrite at high temperatures for technical applications [22]. However, sulfide (S^{2-}) dose, for iron sulfides formation has never been viewed as a GW treatment concept for iron removal. Moreover, nobody has approached pyrite formation under conditions commonly found in GW treatment plants, namely high flows, turbulent hydraulic conditions and relatively short hydraulic retention times (HRT).

1.2 Research Problem & Motivation: Anoxic Iron Sulfides Formation for Iron Removal

This study investigates the novel concept of iron removal via sulfide dosing for the formation of iron sulfides as mechanism for GW treatment. This section highlights why this gap should be addressed and motivates the choice of sulfide dose and pyrite as targeted iron sulfide. Lastly, kinetic considerations concerning pyrite formation are presented indicating the theoretical feasibility of the approach.

Investigating sulfide dosing can path the way for more efficient resource usage. It aims for a paradigm shift, from seeing removed iron as waste to a possible resource. Sulfide can react with iron to form pyrite. This can be employed for sulfuric acid production, which is widely used for fertilizer production [22]. Another product might be mackinawite (FeS_m). FeS_m has the potential for

simultaneous treatment of other contaminants such as arsenic [22]–[24]. Moreover, FeS_m and pyrite are compact compared to iron flocs, taking up, way less space once produced.

There are four more reasons for sulfide addition. Firstly, sulfide is a GW native compound. It originates from the activity of sulfate reducing bacteria [25]–[27]. Subsequently, these sulfides often trigger the precipitation of metal sulfides [28]. Therefore, H_2S concentrations in GW are usually less than 0.1ppm [28] to 1ppm [29]. However, there are locations where GW can have (naturally) occurring elevated H_2S concentrations (0.03-5.11 mg H_2S/L [30], 10-200 mg H_2S/L[31] & 0.9 mg H_2S/L [32]). Secondly, sulfide can potentially be produced electrochemically by reduction of groundwater native sulfate [33], [34]. Moreover, the sulfate concentration often exceeds iron concentrations to such an extent that electrochemical in-situ S^{2-} formation provides enough reactants even for pyrite formation (GW data in [11]). Thirdly, GW treatment plants personnel have experience with H_2S, as this can escape during the aeration process [35]. H_2S-meters are therefore usually in stock. Lastly, excess sulfide possibly leaving an iron-sulfides formation reactor can be removed through pre-existing aeration, removing H_2S concentrations up to 2 ppm [35].

In this study the experiments are designed for the formation of the iron sulfide pyrite. There are two reasons for this. Firstly, even across a wide pH range [36], pyrite is the most stable iron sulfide due to its extreme low solubility product [21]. Secondly, pyrite formation kinetics seem to be fast enough to be employed for groundwater treatment.

The following briefly reviews literature related to kinetic considerations regarding pyrite formation

Pyrite formation is often considered slow. However, experimental pyrite formation studies indicated 12-17 magnitudes faster formation rates than in natural sediments [37]. For illustration, reported experimental pyrite formation rates for the H_2S pathway are up to $2 * 10^{-8}$ [37] and $3 *10^{-6}$ mol pyrite L^{-1} s^{-1} [38], [39]. Converting these pyrite formation rates to iron removal rates results in 0.07 to 10 mg Fe L^{-1} min^{-1}, respectively. Though, it should be acknowledged that these studies were carried out at Fe concentrations significantly higher than the typical few mg Fe/L found in groundwater.

Hence, initial pyrite formation rates calculated by the rate-equation [40] yield in an duration of ca. 630 days for concentrations equaling 20mg Fe/L and 11.5 mg S^{2-}/L. However, another study approaching pyrite formation in the presence of pyrite seeding crystals at similar concentrations (ca. 16mg Fe/L and 11 mg S^{2-}/L) observed average formation rates of $1.6*10^{-8}$ mol L^{-1} s^{-1} [41]. Under aforementioned concentrations of 20mg Fe/L and 11.5 mg S^{2-}/L this would lead to a depletion of reactants after 3h. This is a difference of four magnitudes between the rate-equation and experimentally observed formation rates in the presence of pyrite seeding crystals.

In the latter study, it was argued that the formation rates are surface area dependent [41] and pyrite crystals can catalyze further pyrite formation [42]. Therefore, a column filled with pyrite seeding crystals was used here to enhance catalytic effects leading to increased formation rates as demonstrated by the off set of these two studies.

1.3 Objectives and Research Questions

The aim of this section is to concisely present the target of this investigation. Therefore, this section provides the goal, the main research question, sub research questions and key term explanations. Additionally, it is briefly stated how the research question is aimed to be answered.

Goal:

- Explore anoxic iron removal in GW treatment via iron sulfides formation.

Main Research Question:

- What are the processes by which iron(II) is removed from groundwater anoxically using sulfide addition in an up-flow column reactor filled with pyrite seeding crystals?

Sub-questions

1. Can pyrite form and what mechanisms are influencing its formation under these conditions?
2. What other iron sulfides and products than pyrite may form under these conditions?
3. Where are iron sulfides forming and how are they retained?
4. What is the ratio of removed iron to removed sulfide?

The term “processes” in the main research question relates to the underlying mechanisms and formed phases ultimately leading to the separation of iron from raw groundwater. The “up-flow column reactor filled with pyrite seed crystals” refers to the experimental set-up that was utilized in this investigation and is elaborated on in section 2.2.1.

1.4 Thesis Outline

This section outlines how the research question is addressed and provides an overview of the thesis structure. To conduct the main experiments, a pyrite seeding crystal-filled up-flow column reactor was constructed and supplied with solutions containing iron and sulfide at two different dosing ratios. Chapter 2 provides detailed information on this setup. Additionally, preliminary tests were performed to ensure anoxic operation, achieve the desired pH, and estimate the pore volume. Concentration stabilization tests were conducted to investigate the interaction of iron and sulfide with the pyrite seeding crystals, both individually and in combination. Furthermore, the identification of formed solids using Scanning electron microscopy with an energy dispersive X-Ray analyzation (SEM-EDX), X-Ray diffraction analysis (XRD), and Raman Spectroscopy is described.

Chapter 3 presents the results of the concentration stabilization test, and dose response iron sulfide formation tests investigated with the up-flow column reactor. The chapter also presents the ratios of removed iron to removed sulfide derived from the reactor operation and the analysis of solid phases. In Chapter 4, the results are discussed with respect to the four sub research questions, respectively. Relevant literature was used to understand the underlying mechanisms. The chapter concludes by addressing the significance of the obtained results for groundwater treatment applications. Lastly, Chapter 5 provides conclusions and offers recommendations for further research.

2 Materials & Methods

The overarching goal of all experiments was to explore the novel concept of anoxic iron removal in GW treatment via iron sulfides formation. To investigate this, an up-flow column reactor filled with pyrite seeding crystals was built and fed with iron and sulfide containing solutions. The reactor set-up is illustrated in Figure 2-1. This chapter outlines the materials and methods used in this investigation.

A comprehensive overview of all experiments is presented in section 2.1. The experimental setup and reaction media utilized for the main experiments are detailed in section 2.2, followed by section 2.3 which describes the preparatory experiments required for reactor operation. Information concerning the concentration stabilization tests are provided in section 2.4, whereas section 2.5 explains the main experiment which is the dose response iron sulfide formation test. Analytical methods are listed in section 2.6. Lastly, sections 2.7 and 2.8 describe Phreeqc models developed and the creation of Eh-pH diagrams, respectively.

2.1 Overview Experiments

This section provides an overview of all conducted experiments. These can be distinguished in two categories: preparatory and main experiments and are detailed the subsequent list. Additional information on employed methods and preparatory tests can be found in Appendix B.

- Preparatory Experiments (2.3)
    - Evaluation of anoxic media preparation and anoxic reactor operation (2.3.1)
    - Batch test quantifying acid dosage for pH control (2.3.2)
    - Pore Volume Test (2.3.3)
- Main Experiments
    - Concentration stabilization test (2.4)
        - Sulfide stabilization test
        - Iron stabilization test
        - Iron sulfide stabilization test
    - Dose response iron sulfides formation test (2.5)

2.2 Experimental Set-up

This section aims to provide detailed information about the up-flow column reactor and influent media utilized for the main experiments. All experiments dealing with sulfide were carried out in a fume hood.

2.2.1 Up-flow Column Reactor

This section shows the up-flow column reactor set-up and provides specifications about its components. A scheme of the laboratory reactor is given in Figure 2-1.

Inflatable aluminum-laminate bags (3 & 10L, Unibrew Nederland, Netherlands) were used for storing the influent media and collecting the effluent. The aluminum laminate provides an oxygen barrier to keep the media anoxic. A glass cylinder (117 mL) of 40 cm length with a diameter of 1.9 cm was selected as a reactor. It has a stainless-steel mesh at the inlet and outlet. The reactor was positioned vertical operating in up-flow mode. Peristaltic pumps (120U, Watson-Marlow Fluid Technology Solutions, UK) were used to feed the system.

The reactor was filled with pyrite crystals (Mineraliengrosshandel Hausen GmbH, Austria) sieved for a diameter range of 1.4 to 2.8 mm (mean 2.1 mm). Additionally, two polished cubic pyrite crystals (MIKON GmbH, Germany) were added for scanning electron microscopy analysis. Watson Marlow Marprene tubing was used for the pumps (902.0016.016, Watson Marlow, UK). All remaining tubing were made of polyurethane (PUN-H-6X1-SW, Festo, Germany),

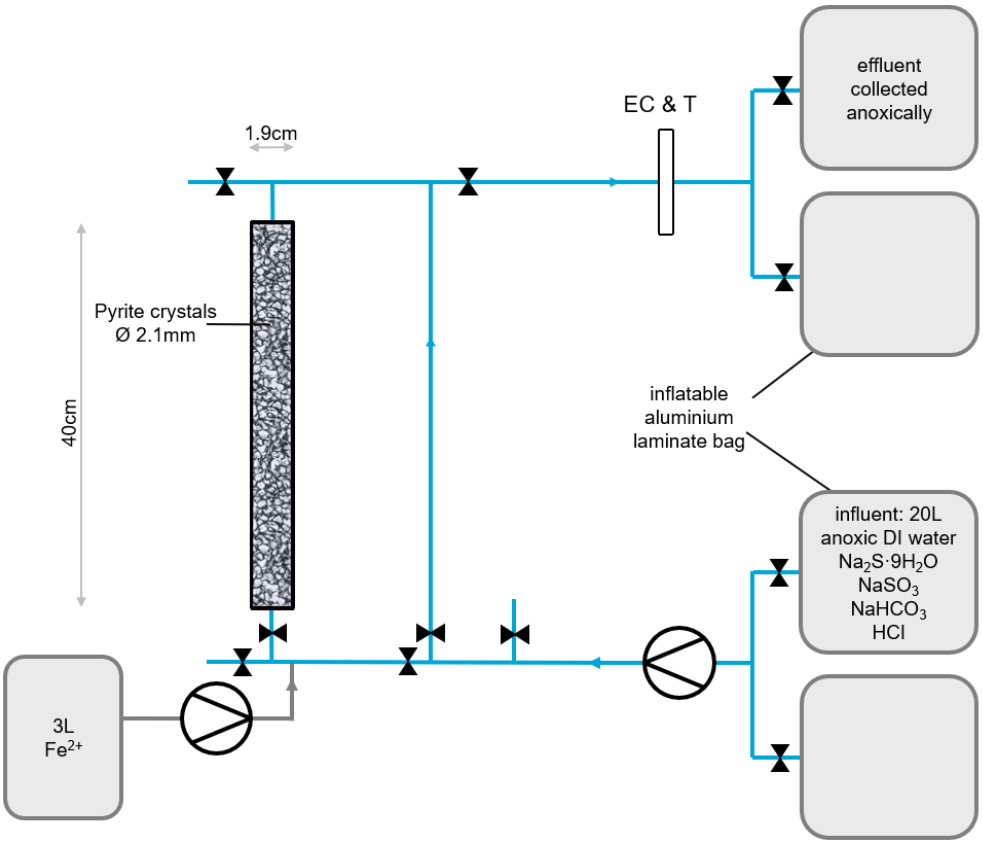

Figure 2-1 Scheme of lab-scale up-flow column reactor for iron sulfides formation. Rectangle labelled with "EC & T" represents electrical conductivity (EC) and temperature (T) probe. Sampling ports are indicated before and after the reactor in- and outlet, respectively.

2.2.2 Influent Media

This section shows the composition of the influent media. All chemicals used were of ACS Grade or higher. Suppliers of all chemicals can be found in the Appendix (page 49).

All media were sparged with N_2-gas until an oxygen concentration of <0.02 mg O_2/L was reached. Mohr's salt ($(NH_4)_2Fe(SO_4)_2·6H_2O$) was used as iron(II) source, as it is reported, that Fe(II) from this salt is more resistant to oxidation compared to other Fe(II) salts [20]. $Na_2S·9H_2O$ was utilized as

sulfide source [43]. There is little chemical difference between utilizing Na_2S, NaHS or H_2S+ NaOH, with respect to iron sulfides formation studies [20]. Sodium sulfite was utilized as oxygen scavenger and $NaHCO_3$ was dosed as a pH buffer. The pH was adjusted with HCl (2.3.2). An overview of the calculated ionic compositions for each experiment is given in Table 2-1.

Table 2-1 Calculated ionic composition of mixed influent media for concentration stabilization test and dose response iron sulfides formation test.

Constituent	Preliminary Experiments	Concentration Stabilization test			Dose Response Iron Sulfides Formation Test	
	Anoxic Prep & Pore Volume Test	Sulfide Stab.	Iron Stab.	Iron Sulfide Stab.	Dose $Fe:S^{2-}$ = 1:1	Dose $Fe:S^{2-}$ = 1:2
	[mg/L]	[mg/L]	[mg/L]	[mg/L]	[mg/L]	[mg/L]
Fe^{2+}	-	-	20	20	20	20
Na^+	93	97	93	110	110	126
HCO_3^-	171	171	171	171	171	171
SO_3^{2-}	58	58	50	50	50	50
SO_4^{2-}	-	-	69	69	69	69
S^{2-}	-	11.5	-	11.5	11.5	23
NH_4^+	-	-	13	13	13	13
Cl^-	-	92	92	92	92	102
pH_{meas} [-]	-	6.9	5.7	6.1 ± 0.1	6.1 ± 0.1	6.0
$EC_{eff,meas}$ [µS/cm]	503 ± 2	560 ± 45	641 ± 3	703 ± 14	682 ± 19	723 ± 49

2.3 Preliminary Experiments

This section shows the description of the preliminary experiments. The aim of these experiments was to evaluate the oxygen and pH control. Furthermore, they investigated the pore volume to estimate the HRT.

2.3.1 Anoxic Operation

The aim of this preliminary experiment was to check whether the system stays oxygen free over a run-time of a few days. Two experiments were done: (i) Evaluation of anoxic media preparation and reactor operation and (ii) evaluation of the oxygen barrier of the aluminum laminate bags.

For the first experiment the “preliminary experiment media “ (Table 2-1) was used and prepared in the same manner as the sulfide containing media. Subsequently, it was connected and fed to the system for three days. No iron was dosed, and no pyrite was present in the reactor. The oxygen concentration was monitored continuously at the position of the EC probe indicated in Figure 2-1.

For the second experiment, the same media was prepared and stored in an aluminum laminate bag for two weeks. Afterwards, it was fed to the system and again the dissolved O_2 concentration was measured.

For both experiments the oxygen concentration was constantly <0.05 mg O_2/L. The media preparation was therefore seen satisfactory.

2.3.2 Acid Dosage Quantification for pH Control

The purpose of this experiment was to identify the amount of hydrochloric acid needed to reach a pH of 6.5 for the mixed influent.

The two influent solutions (Figure 2-1) were mixed in a spinner flask in the same ratio as in the reactor summing up to 500 mL. The pH was continuously measured and a 0.2M HCl solution was dosed until the pH reached 6.5 under constant stirring. The test was done for the two different sulfide concentrations used. The ultimate HCl dosage is reflected in the Cl^- concentration in Table 2-1, since no other Cl^- source was used.

2.3.3 Pore Volume Test

The aim of the pore volume test was to identify the porosity to estimate the HRT. Two methods were used to estimate the pore volume. One based on a tracer dosage and the second one based on physical considerations.

Tracer Method

The reactor was filled with pyrite crystals and the “preliminary experiment media “ (Table 2-1) was fed to the system from the main influent side. The electrical conductivity was continuously measured in the effluent and after the EC had stabilized a highly concentrated tracer solution (NaCl) was dosed from the iron dosing point (Figure 2-1). The pore volume was then calculated according to equation (2).

$$V_{pore} = \left(T_{50} - \frac{V_{tubes}}{Q}\right) * Q \qquad (2)$$

With
V_{pore} = Pore volume [mL],
T_{50} = Duration from EC_{start} till EC_{50} (EC_{50} = ½ (EC_{start} + EC_{max})) [min],
V_{tubes} = Volume of tubes between dosing point and column + volume of tubes between end of column and EC sensor [mL]
Q = inflow [mL/min]

Physical considerations method

For the physical consideration’s methods, the pore space was calculated according to equation (3).

$$V_{pore} = V_{col} - \left(\frac{m_{pyrite}}{\rho_{pyrite}}\right) \qquad (3)$$

With
V_{pore} = pore volume [mL]
V_{col} = volume of column [mL]
m_{pyrite} = mass of pyrite in column [g]
ρ_{pyrite} = density of pyrite [5.02 g/mL] [44]

V_{col} was estimated by filling the column with water followed by measuring the volume of the drained water. m_{pyrite} was derived by weighing the column before and after filling it with pyrite seeding crystals.

The pore volume estimated by the tracer and physical considerations method equals 58mL and 56.5mL, respectively. A pore volume of 57mL was used for the calculations. This equals a porosity of 0.49.

2.4 Concentration Stabilization Tests

The aim of these experiments was to identify, how often the filled pore volume has to be replaced[1] to reach steady effluent concentrations for the dosed sulfide and iron. Additionally, this study investigated the individual and combined interactions of iron and sulfide with the pyrite seeding crystals. Hence, three tests were carried out, an iron, sulfide and iron sulfide stabilization test. These are described in the subsequent paragraphs.

During the iron stabilization test the column was filled with pyrite seeding crystals. The iron stab. media (Table 2-1) was fed to the system. Samples were taken over time at the influent and effluent sample port of the reactor and analyzed for iron (see section 2.6.1).For the sulfide concentration stabilization test, the same conditions were used. Though, the sulfide stab. media (Table 2-1) was fed to the system at the feeding rate of 185mL / hour and therefore HRT of 19min. Lastly, for the iron sulfide stabilization test the iron sulfide stab. media (Table 2-1) was dosed.

2.5 Dose Response Iron Sulfides Formation Test

The aim of this experiment was to investigate the approach of iron sulfides formation for iron removal in groundwater treatment. Moreover, it aimed to identify the molar ratio of removed iron to removed sulfide (Fe_{rem}:S^{2-}_{rem}). Experimental conditions were chosen to favor and enable pyrite formation. It is the main experiment of this thesis and utilizes the reactor set-up illustrated in Figure 2-1.

The reactor was fed with iron and sulfide containing solutions. Two molar dosing ratios were tested, Fe:S^{2-} = 1:1 and 1:2, respectively. The respective reactor influent compositions can be found in Table 2-1.

The reactor was filled with pyrite crystals to catalyze the formation of new pyrite crystals [41], [42] and to provide surface area for crystal growth. To estimate the HRT an equation was established that approximates pyrite formation rates accounting for surface catalytic effects. This differs from solely assessing formation rates based on the rate equation that relies on reactant concentrations. The HRT was therefore calculated by equation (4).

$$HRT = \frac{Q}{V_p} = \frac{\frac{R_p}{c_{Fe}} * A_p}{V_p} \quad (4)$$

with
HRT = Hydraulic Retention Time [s],
Q = reactor inflow [m³/s],
V_p = pore volume [m³],
R_p= pyrite crystal growth rate [mol FeS_2 /(m² s)],

[1] One pore volume = time until pore volume water has been replaced once = HRT

A_p = active surface area of pyrite seed crystals [m²] and
c_{Fe}= Iron concentration that can pot. be removed based on sulfide dosage and assuming only pyrite is formed [mol Fe/L],

The assumed crystal growth rate (R_p), 5.4 x 10^{-5} mmol/(m² s), is the average pyrite crystal growth rate of the four hour long experiment [41]. Their study used similar initial iron and sulfide concentrations (about 16 mg Fe^{2+}/ L and 10.6 , mg S^{2-}/L).
Smooth spherical particle shapes were assumed for quantifying the active surface area of pyrite seeding crystals (A_p) instead of using the specific surface area measurement (2.6.2). This was done to increase the robustness of the estimates. It therefore aims to account for wall effects and preferential flow, which can significantly decrease the actual active catalytic surface area of the pyrite seeding crystals.
The HRT time was calculated for the Fe:S^{2-} ratio = 1:1. The same HRT was used throughout the whole experimental run-time, independently of the Fe:S^{2-} ratio.
The iron concentration that could potentially be removed based on the sulfide dosage and assuming only pyrite is formed (c_{Fe}) was 0.18 mmol Fe^{2+}/L (10mg Fe^{2+}/L).

Based on equation (4) an HRT of 19 minutes was estimated. The reactor inflow was therefore ca. 185mL/ hour.

2.6 Analytical Methods

This section shows the analytical methods for determining the dissolved water constituents (2.6.1) and solid phases in the reactor system (2.6.2).

2.6.1 Analysis of Dissolved Constituents

Table 2-2 gives an overview of methods used to analyze dissolved water constituents. The sampling procedure can be found in Appendix C (p. 48).

Table 2-2 Methods and devices used for analysis of water parameters.

Parameter	Method/Device
Fe^{2+}	Hach method LCK 320 & LCK321 (Hach Lange GmbH, Germany)
S^{2-}	Methylene blue method → Hach method LCK653 (Hach Lange GmbH, Germany)
O_2	Optical IDS dissolved oxygen sensor FDO® 925 (Xylem Analytics, USA)
pH	InPro 3250i/SG/225 (Mettler Toledo, Switzerland) – sulfide resistant IDS pH-Electrode SenTix® 940 (Xylem Analytics, USA)
EC	TetraCon® 925 (Xylem Analytics, USA)

Some sulfide samples were conserved by immediate addition of zinc acetate and NaOH for later analysis [45]. Until analysis they were stored in the fridge. Conservation stabilizes the samples for at least seven days [46]. Successful conservation was confirmed by here applied measurements (Appendix B, p. 48). If not otherwise specified, uncertainty ranges indicate the standard deviation.

2.6.2 Analysis of Solid Phases in Reactor System

This section specifies the analysis of solid phases from the reaction system. Two kinds of solids can be distinguished that were analyzed: Effluent suspended solids which got flushed out from the reactor and pyrite seeding crystals. Effluent suspended solids were analyzed with XRD, and Raman Spectroscopy. Pyrite seeding crystals were analyzed with SEM, SEM-EDX and a digital microscope. Furthermore, the surface area was estimated for the pyrite seeding crystals.

2.6.2.1 Collection of Effluent Suspended Solids

Effluent was collected for a period of multiple hours before analysis using aluminum laminate bags. Bags were first flushed with N_2-gas and then evacuated before being connected to the system.

Effluent was filtered with A Nalgene™ Reusable Filter Unit (Thermo Fisher Scientific Inc., USA) with three openings on top. After placing the 0.1µm filter (Cyclopore Track Etched Membrane, Whatman, USA) the headspace was flushed with N_2 gas for five minutes. The effluent bag was directly connected to the top part of the filter unit and the media was filled to the filter unit. During the whole experiment N_2 was flushing the headspace to keep the media anoxic.

After filtration, the filters were immediately moved to an anoxic chamber (Coy Laboratory Products, Inc., USA) where they were allowed to dry prior to analysis.

2.6.2.2 XRD

X-ray diffraction analysis was carried out using a D8 Advance Eco (Bruker Corporation, USA) to identify any formed crystallographic structure that flushed out from the up-flow column reactor. Analysis was performed on the solids retained on the discs. XRD patterns, in the range of 5-90° 2θ, were collected under air using the following settings: 0.6mm receiving slit, 0.1s/0.0103° 2θ counting time.

2.6.2.3 Raman Spectroscopy

Raman spectroscopy was carried out using a Renishaw Invia Reflex (Renishaw, UK). Solids retained on the filter paper were analyzed under the following settings: 515 nm, 1% I of 50mW, 20 acc, dwell time 2s , center range 1050 cm^{-1}.

2.6.2.4 Digital Microscope

A digital microscope was used to take pictures of the pyrite seeding crystal prior and after the experiments. Pyrite crystals were dried in silica desiccants containing anoxic chamber. A VHX-500 digital microscope (Keyence Corporation, Japan) was used.

2.6.2.5 SEM & SEM-EDX

Scanning electron microscopy with an energy dispersive X-Ray analyzation was conducted on two polished cubic pyrite crystals to investigate whether any crystal growth, mineral depositing or surface transformation had occurred on the seeding crystals. Crystals were analyzed before and after the experiments. A NovaNano SEM (FEI, USA) was used for analyzation.

Before the experiments pyrite crystals were immersed in 0.4M HCl for ten minutes followed by polishing with a wool felt and subsequent cleaning with deionized (DI) water.

After the experiments pyrite crystals were taken from the reactor after draining the remaining anoxic water by flushing the column with N_2-gas. The column was then sealed and moved to the anoxic chamber to withdraw the polished cubic pyrite crystals.

Half of the analyzed cubes face was cleaned gently using a cosmetic tissue followed by rinsing with DI water. Afterwards the cubes got immediately freeze dried and were Au-coated prior to analysis.

2.6.2.6 Surface Area Estimation

The surface area was estimated to approximate the formation rates for calculating the desired HRT (2.5). Two techniques were utilized to determine the surface area, one based on the weight, density and assumption of spherical geometry of the pyrite crystals, and the other based on the standard method according to the Brunauer, Emmett and Teller (BET) theory [47].

According to the first method the surface area equals $5.7 * 10^{-4}$ g/m^2 (tot. = 0.16m²). Measurements according to the BET theory gave a value of 0.036 ± 0.011 m²/g (tot. = 10.8m²).

2.7 Phreeqc Models

Phreeqc [48] models were used to simulate the effect of sulfide dose on the redox potential and to derive the equilibrium solubility of mackinawite. Furthermore, they were used to calculate the saturation index (SI) of pyrite. Source codes are provided in Appendix E. The database “phreeqc.dat” was used for all simulations.

2.8 Eh-pH Diagrams

Eh-pH (Pourbaix diagrams) were created with Geochemist Workbench [49]. If not otherwise specified, the “Iron Sulfide Stab.” media composition specified in Table 2-1 were used for running the calculations.

3 RESULTS

The aim of all experiments was to explore the concept of anoxic iron removal in GW treatment through the formation of iron sulfides and to understand the underlying mechanism. This chapter presents the findings of the experiments conducted with the pyrite-filled up-flow column reactor to investigate this concept.

Firstly, concentration stabilization tests are shown for iron and sulfide individually and combined (3.1). Section 3.2 continues with showing the effects of different sulfide doses on iron retention under steady conditions. Ratios of removed iron to removed sulfide are given in section 3.3. Lastly, section 3.4 provides the results of the solid phase analysis.

3.1 Concentration Stabilization Tests

The aim of the concentration stabilization tests was to identify how many pore volumes it takes to reach steady effluent concentrations for the dosed sulfide and iron individually and combined. Additionally, the interactions of iron and sulfide with the pyrite seeding crystals, both individually and in combination, were investigated.

3.1.1 Sulfide Stabilization Test

This section provides the experimental data of the sulfide stabilization test. Results are shown in Figure 3-1 portraying the in- and effluent concentrations until equalization. Effluent sulfide almost equaled influent sulfide concentrations after ca. 360 pore volumes.

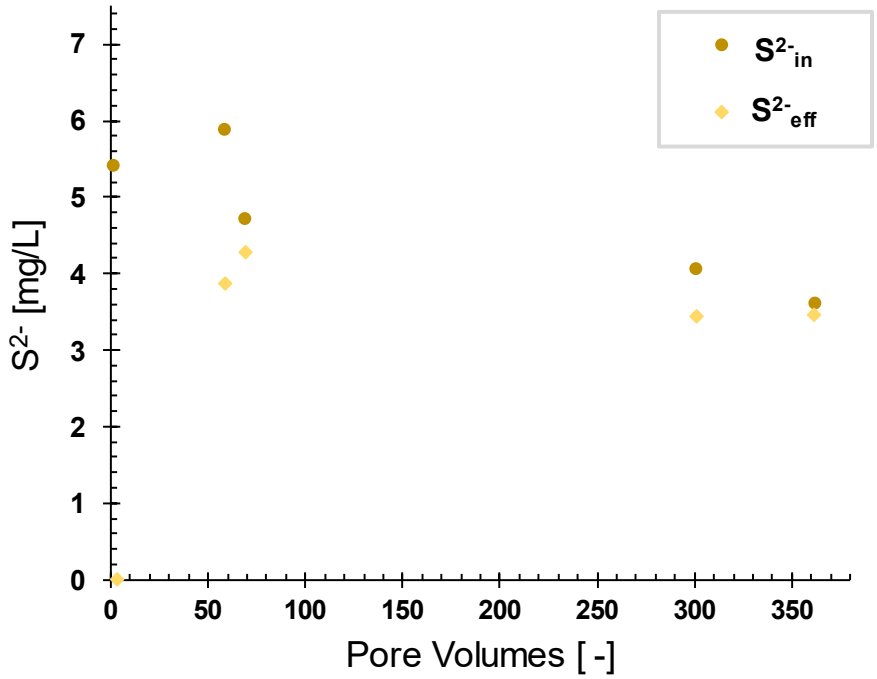

Figure 3-1 Sulfide concentration stabilization test. Pyrite filled up-flow column reactor fed with "Sulfide Stab." media (Table 2-1). No iron dose. HRT = 19min.

After ca. 70 pore volumes effluent sulfide concentrations nearly equaled influent concentrations (Δ=about 0.4 mg S^{2-}/L). Ultimately, the effluent nearly equaled the influent concentration after 360 pore volumes, showing a difference of ca. 0.1 mg S^{2-}/L. This was considered sufficient to assume no constant off set or ongoing interaction between the sulfide and pyrite. Although, it cannot be excluded that the deviation between in and effluent concentrations from pore volume 70 onwards only decreased due to the uncertainty range of the S^{2-} quantification method.

3.1.2 Iron Stabilization Test

This section shows the data of the iron stabilization test. Results are shown in Figure 3-2 indicating in- and effluent iron concentrations. The effluent iron concentration stabilized after ca.110 pore volumes.

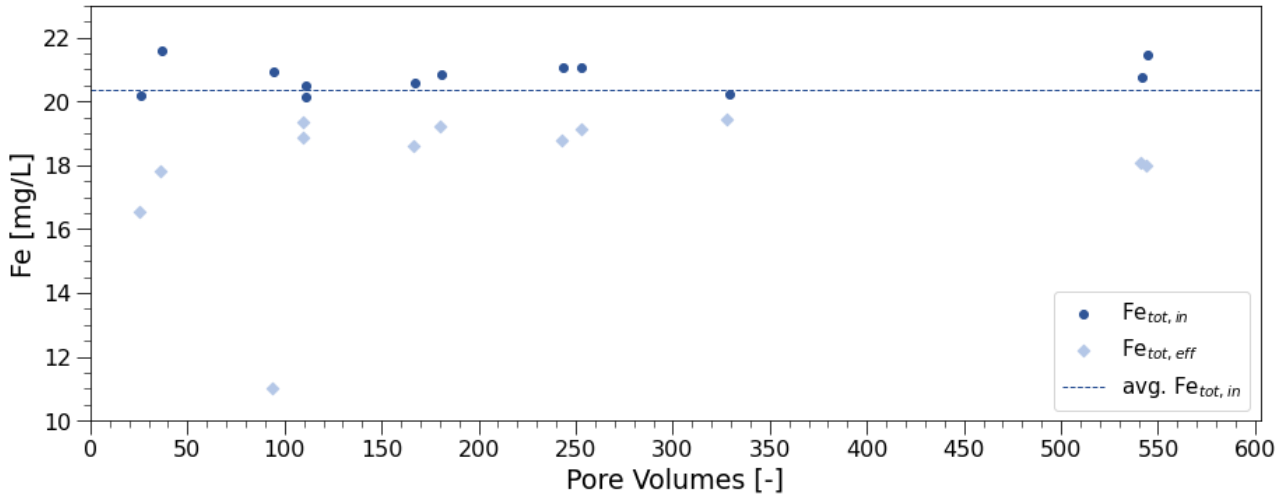

Figure 3-2 Iron concentration stabilization test. Pyrite filled up-flow column reactor fed with "Iron Stab." Media (Table 2-1). No sulfide dose. Avg. $Fe_{tot,in}$ = 20.3 ± 1.3 mg Fe/L over whole run time. X-axis shows number of pore-volumes. HRT = 19min.

The in- and effluent oxygen concentrations were 0.48 mg O_2/L and 0.06 mg O_2/L at 550 pore volumes. This occurred despite extensive preliminary tests evaluating anoxic conditions (2.3). Applying stoichiometries of iron oxidation by oxygen, the resulting offset between in- and effluent oxygen of 0.42 mg O_2/L is sufficient for oxidation ca. 3 mg Fe^{2+}/L. The off-set between influent to effluent iron at 550 pore volumes equals ca. 3 mg Fe/L.

An estimated 83 mg Fe accumulated in the column during the iron stabilization test. The mass balance neglected the third effluent Fe value shown in Figure 3-2. Since this is considered an outlier.

3.1.3 Iron Sulfide Stabilization Test

Figure 3-3 displays the data from the iron sulfide stabilization test, which includes measurements of sulfide and iron concentrations in both influent and effluent. Iron was retained in the pyrite filled up-flow column reactor, after an initial phase of iron release spanning approximately 540 pore volumes.

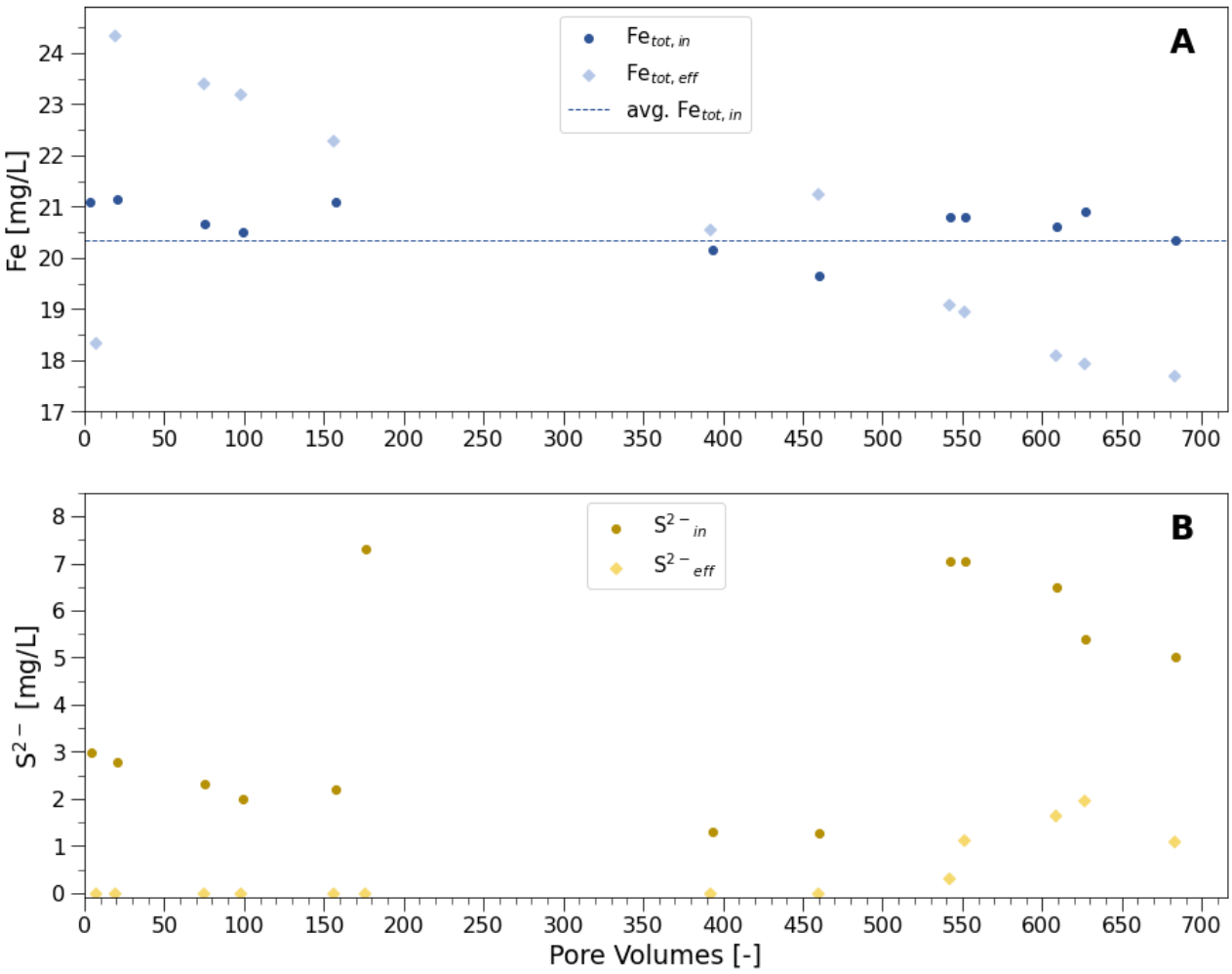

Figure 3-3 Effluent and influent iron (A) and sulfide (B) concentrations during the start-up phase of the pyrite filled up-flow column reactor. Avg. $Fe_{tot,in}$ = 20.3 ± 1.3 mg Fe/L over whole run time. Reactor fed with "Iron Sulfide Stab." media (Table 2-1). HRT = 19min.

This test was carried out after the iron stabilization test (3.1.2). Therefore, previously retained iron was still present in the up-flow-column reactor. Iron started to be released when sulfide dose was started. This is illustrated by the first two sample points. Effluent iron concentrations raised from 18.4 to 24.4 mg Fe/L (Figure 3-3 A).

Iron was released from the up-flow column reactor until ca. 540 pore volumes. Note that during this period no sulfide could be detected in the effluent independently of the incoming sulfide concentration (Figure 3-3 B). Once iron started to be retained (ca. 540 pore volumes), sulfide concentrations did not reach zero anymore.

The last five sampling time points illustrated in Figure 3-3 (data between pore volume 540-700) equal the first five sampling time points illustrated in Figure 3-4 (pore volume 40-200). The fluctuation of the influent sulfide concentration was related to the sensitivity of media preparation.

3.2 Dose Response Iron Sulfides Formation Test

This section indicates the relation between iron retention and sulfide dosage, demonstrated by the dose-response iron sulfide formation test. The purpose of this test was to evaluate the potential for iron removal through sulfide dosing via the formation of iron sulfides. Figure 3-4 shows the in- and effluent iron and sulfide concentrations under molar dosing ratios of $Fe:S^{2-}$ = 1:1 and 1:2,

respectively. The results indicate that iron is retained by sulfide dosage, and that increasing sulfide doses lead to greater levels of iron retention.

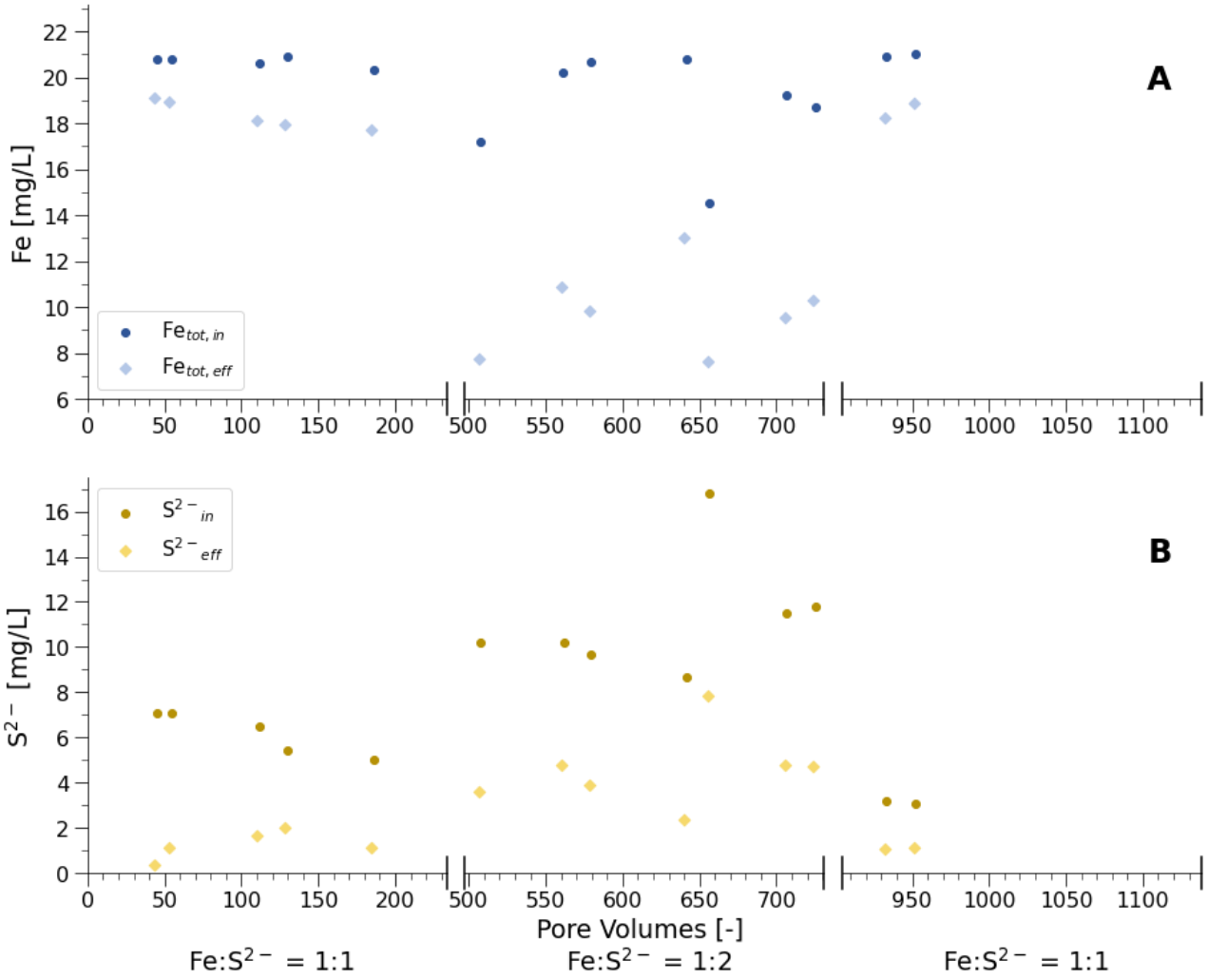

Figure 3-4 Dose response iron sulfides formation test at molar Fe:S^{2-} dosing ratios of 1:1 (left and right) and 1:2 (center). A: Fe in- and effluent concentrations. B: In- and effluent S^{2-} concentrations. Reactor fed with Fe:S^{2-} = 1:1 & 1:2 media, respectively (Table 2-1). HRT = 19min.

The data included in Figure 3-4 shows values for stable conditions at the respective dosing ratios. The whole timeline of reactor operation can be found in Appendix A (p.41).

Increased sulfide doses co-occur with increased iron retention in the up-flow column reactor. The Fe:S^{2-} = 1:2 dosing ratio lead to an average effluent concentration of 9.9 ± 1.5 mg Fe/L (center Figure 3-4), while an effluent concentration of 18.4 ± 0.5 mg Fe/L (left & right Figure 3-4) was observed for the 1:1 dosing ratio.

Effluent sulfide concentrations specified in Figure 3-4 B include FeS bound sulfides. This was evaluated in an experiment and is detailed in Appendix B (p. 48). Thus, it remains unclear whether all sulfide has reacted and was not retained or whether it has not entirely reacted with the Fe^{2+}.

The pH for the Fe:S^{2-} = 1:1 dosing ratio was 6.1 ± 0.1 and no differences could be observed between the in- and effluent values. The pH for the Fe:S^{2-} =1:2 dosing ratio was 6.0 and 5.9, for in- and effluent respectively.

The influent iron levels at pore volumes 505 and 650 exceed the range of the standard deviation for influent iron values (20.3 ± 1.3 mg Fe/L) considerably, equaling 17.2 and 14.5 mg Fe/L, respectively.

Furthermore, there is an approximate two-fold difference between the intended S^{2-} influent concentration (Table 2-1) and the observed S^{2-} concentration Figure 3-4.

3.3 Removed Iron to Removed Sulfide Ratios

This section aims to illustrate the ratio of removed iron to removed sulfide during the dose response iron sulfide formation test. The removal-ratios for both sulfide dosing-ratios are presented in Figure 3-5. Higher levels of removed iron per removed sulfide were observed for dosing ratio of $Fe:S^{2-}$ = 1:2 compared to $Fe:S^{2-}$ = 1:1.

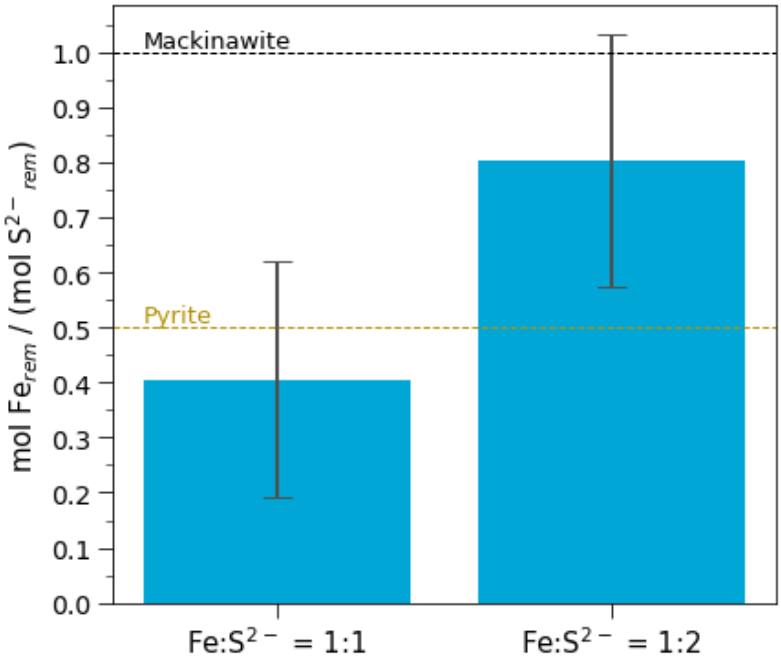

Figure 3-5 Molar ratios of removed iron to removed sulfide. Error bars indicate the standard deviation. X-values show the molar ratios of dosed iron to dosed sulfide. Horizontal lines show molar ratios of Fe:S for mackinawite (FeS_m) and pyrite ($FeS_{2,p}$).

The removed iron and sulfide concentrations shown in Figure 3-5 were calculated for each time point by subtracting the respective effluent from the influent concentration. The absolute standard deviation is ca. 0.2 for both dosing ratios. This results in relative standard deviations of 50% and 25% for $Fe:S^{2-}$ = 1:1 and 1:2, respectively. Furthermore, the ratios need to be interpreted cautiously. This is elaborated on in section 4.4.

3.4 Analysis of Solid Phases in Reactor System

The aim of the solid phase analysis was to identify the formed undissolved constituents to understand which formation mechanisms occurred under the investigated conditions. This section shows the results of the analysis. Flushed out solids were retained on a 0.1µm filter and analyzed with XRD and Raman spectroscopy. Pyrite seeding crystals were analyzed with SEM-EDX and a digital microscope at the end of the experiments.

3.4.1 XRD Analysis of Effluent Suspended Solids

The XRD-analysis aimed to identify any crystalline structure that got flushed out from the up-flow column reactor. Recorded XRD-patterns for the analyzed filter residues are presented in Figure 3-6. No crystalline structures could be observed.

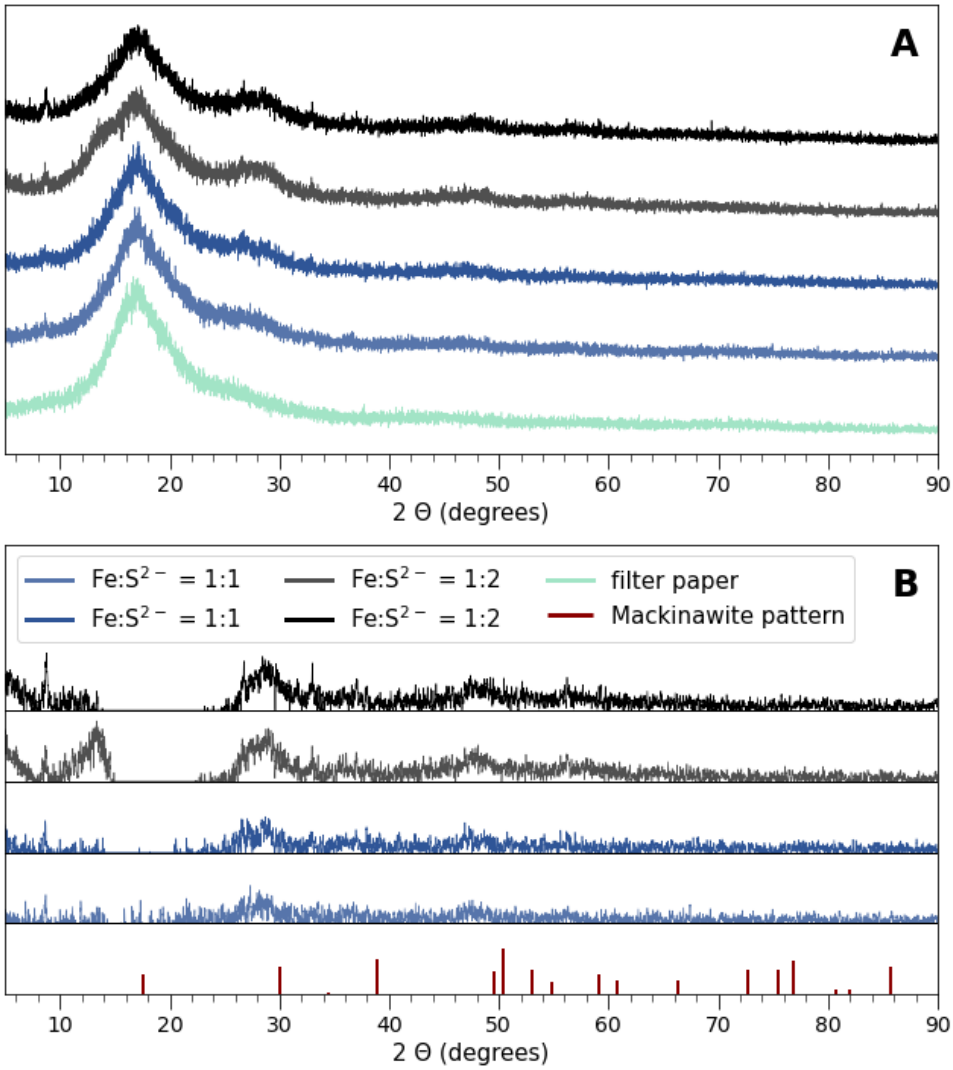

Figure 3-6 XRD pattern of effluent suspended solids retained on a 0.1 µm filter. Y-axis shows the relative intensity (arbitrary unit). Top (A) XRD- patterns of the filter paper and the retained suspended solids at different dosing ratios as a running average (± 0.0516°). Bottom (B) XRD-patterns of suspended solids subtracted by the XRD pattern of the filter paper. Only positive values displayed, no running average applied.

No crystalline structure such as pyrite could be detected in the effluent. For reference, XRD patterns of pyrite seeding crystals used in this investigation can be found in Appendix A (Figure A-2). Furthermore, XRD pattern of oxidized filter residues from a trial before the filtration method was established are found in Appendix A (Figure A-3). The latter seemed to proof the presence of the iron oxyhydroxide lepidocrocite.

3.4.2 Raman Spectroscopy of Effluent Suspended Solids

Raman spectroscopy was used as complimentary technique to XRD for identifying the solids flushed out from the up-flow column reactor. Recorded spectra of the analyzed filter residues are shown in Figure 3-7 A next to reference spectra from literature (Figure 3-7 B). Rhombic sulfur (α-S^8) and pyrite were detected.

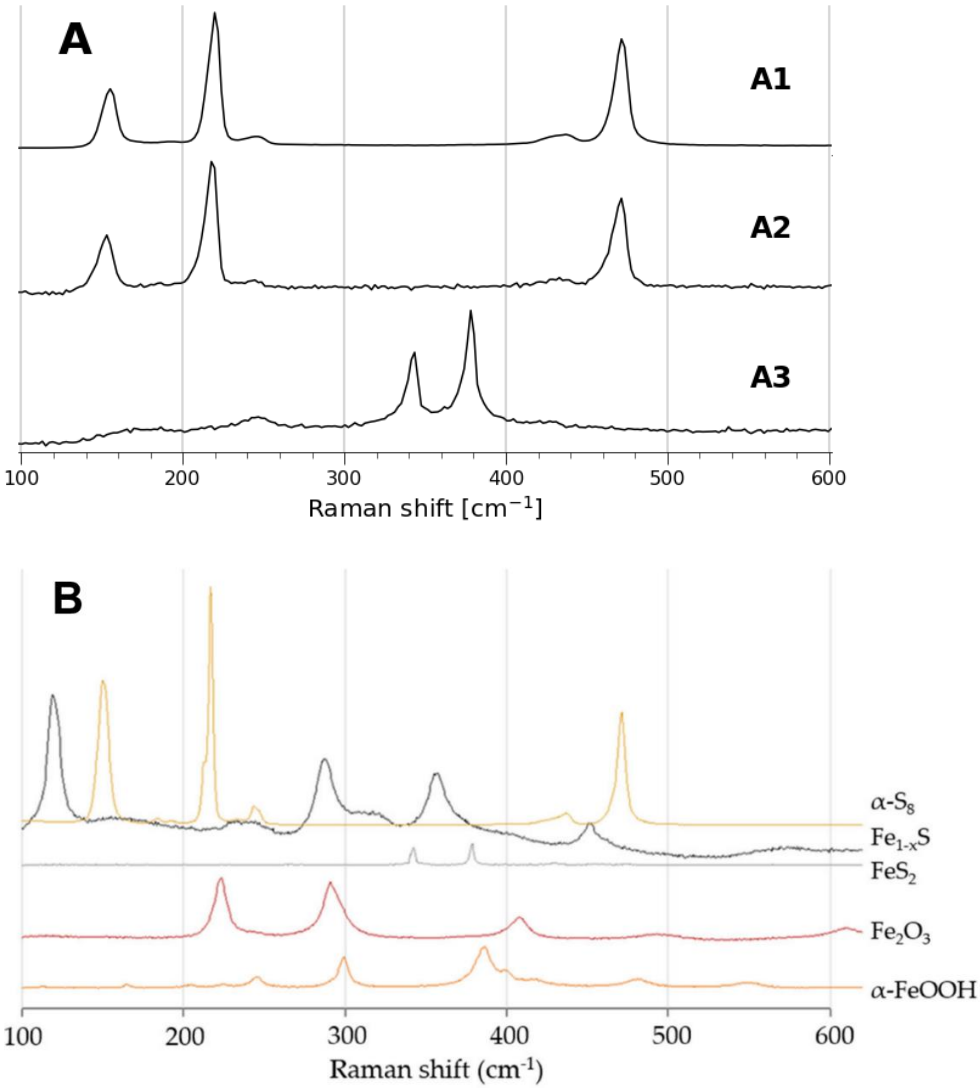

Figure 3-7 Raman pattern of effluent suspended solids (A) and reference pattern for possibly occurring substances from literature (B) [50]. A1-A3 were retrieved from solids retained during the dosing ratio of Fe:S^{2-} = 1:2 from two different samples at three different locations.

Spectra A1 and A2 (Figure 3-7) show a high similarity with the Raman spectra for rhombic sulfur (α-S^8) specified by [50]. The spots from which the spectra were retrieved appeared to be light in color, especially in contrast to its surroundings.

Spectra A3 (Figure 3-7) matches well with the spectra provided for FeS_{2p} by [50]. Similarly, to A1 and A2, the spectra was retrieved from a relatively light location.

Most analyzed locations did not result in identifiable Raman spectra. Three more Raman spectra showing weak peaks are provided in Appendix A (p.43). Mind, that all of these were retrieved from the effluent collected during the high dosing ratio of Fe:S^{2-} = 1:2. For the lower ratio of Fe:S^{2-}= 1:1 no location delivered an interpretable Raman spectrum.

3.4.3 Digital Microscopes Images of Pyrite Seeding Crystals

The digital microscope images aim to illustrate the formed solids retained on the seeding crystals. For this, pictures of pristine pyrite seeding crystals and recovered crystals after reactor operation are provided in Figure 3-8.

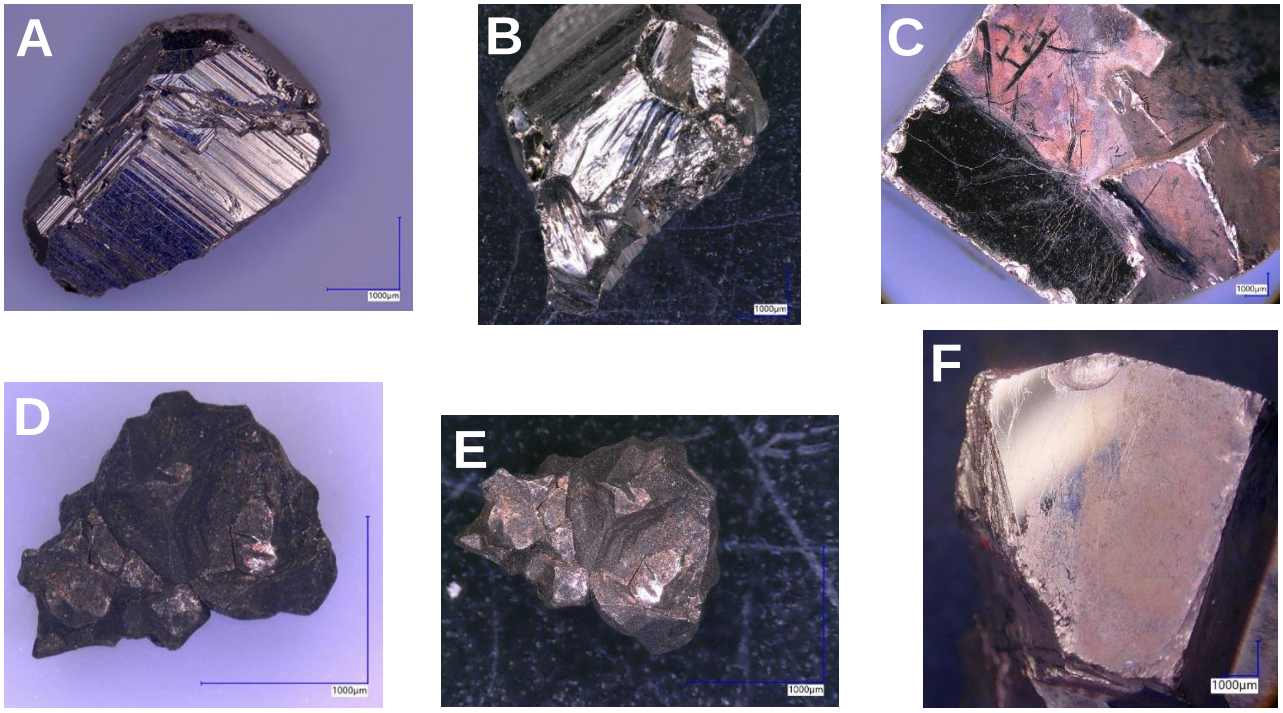

Figure 3-8 Digital microscope images of pyrite seeding crystals. Pristine pyrite crystals on white and black background, respectively (A, B). Pyrite seeding crystals recovered at the end of reactor operation on white and black background, respectively (D, E). Polished pyrite cubes recovered at the end of reactor operation, ca. half of the surface gently wiped off with cosmetic tissue and rinsed with anoxic DI-water (C, F).

Clear black deposits can be seen on the pyrite seeding crystal recovered after the experiments (Figure 3-8 D, E) compared to the pristine ones (Figure 3-8 A, B). Furthermore, the formed deposits could easily be wiped off from the seeding crystals, which is illustrated in (Figure 3-8 C, F). Shiny areas were gently cleaned and appeared like they did before the experiments. However, to proof whether new crystal layers had developed, SEM images were obtained. These are shown in the next section.

3.4.4 SEM and SEM-EDX Images of Pyrite Seeding Crystals

The objective of the SEM and SEM-EDX analyses was to examine potential occurrences of crystal growth, mineral deposition, and surface transformation, as well as to determine the elemental composition of the surface. Figure 3-9 shows the polished pyrite crystal surface before and after the experiment. Reference SEM images of mackinawite and lepidocrocite are shown in Figure 3-10. Figure 3-11 shows the images of polished pyrite crystals recovered at the end of the reactor operation. These were used for SEM-EDX analysis to derive the elemental composition on the surface. SEM-EDX analysis revealed the presence of sulfur and iron minerals on the pyrite seeding crystals. No evidence of pyrite crystal growth was found.

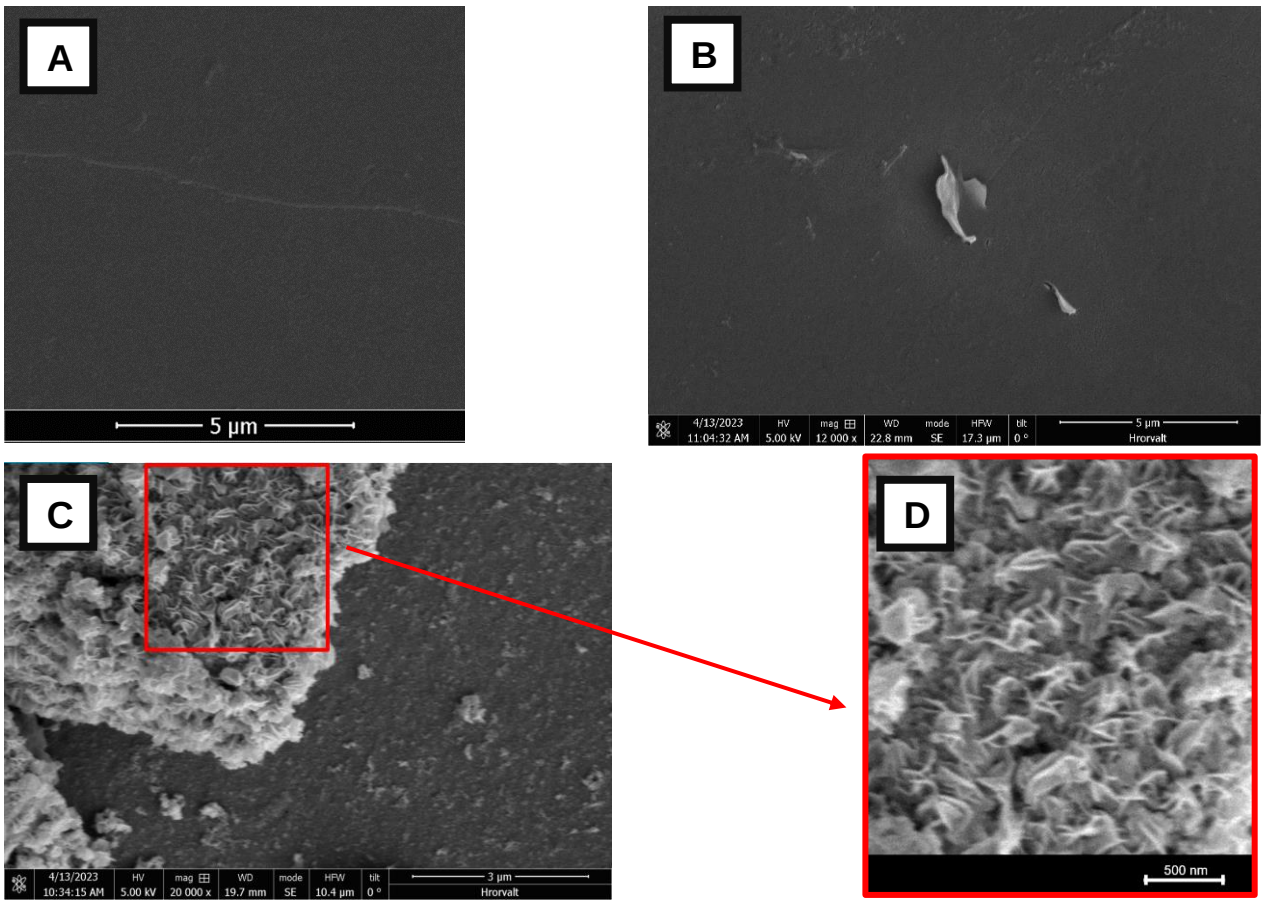

Figure 3-9 SEM images of polished pyrite surface before the experiment (A). Images after the experiment of gently wiped and rinsed (B) and solely rinsed side (C). D shows an amplification of C.

Only loose deposits accumulated at the crystal surface and no crystal growth could be detected. This is illustrated by comparing Figure 3-9 A with B. A shows the polished surface before the experiments and B shows the surface which got wiped off and rinsed gently after the experiments. They barely show any deviation. The white leaf like shape in the center is most likely an irregularity of the crystal itself.

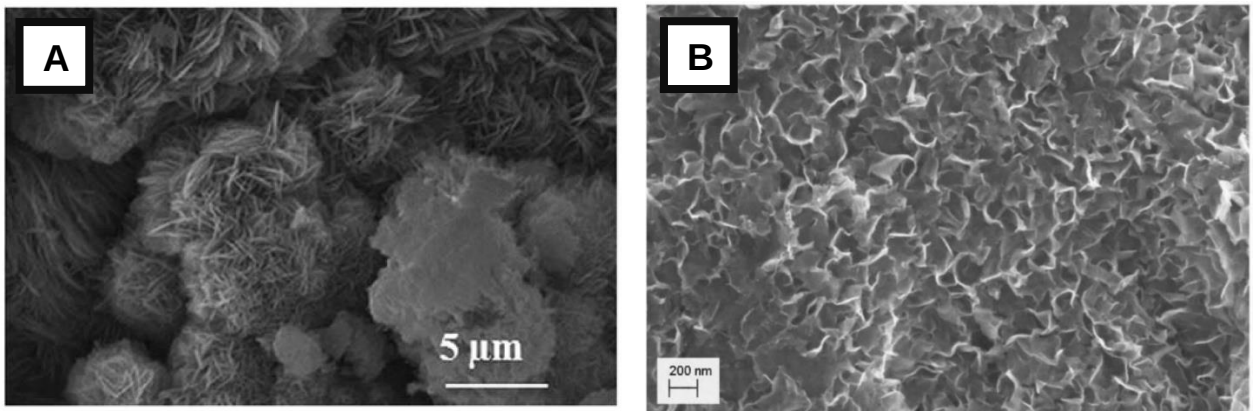

Figure 3-10 Reference SEM pictures of lepidocrocite (A) [51] and mackinawite (B) [52] from literature

The average ratio of Fe:S detected at the surface of the pyrite crystals using SEM-EDX was Fe:S = 1:4.5 ± 0.6 (n=4). For comparison pyrite would yield in a ratio of 1:2 and mackinawite in 1:1.

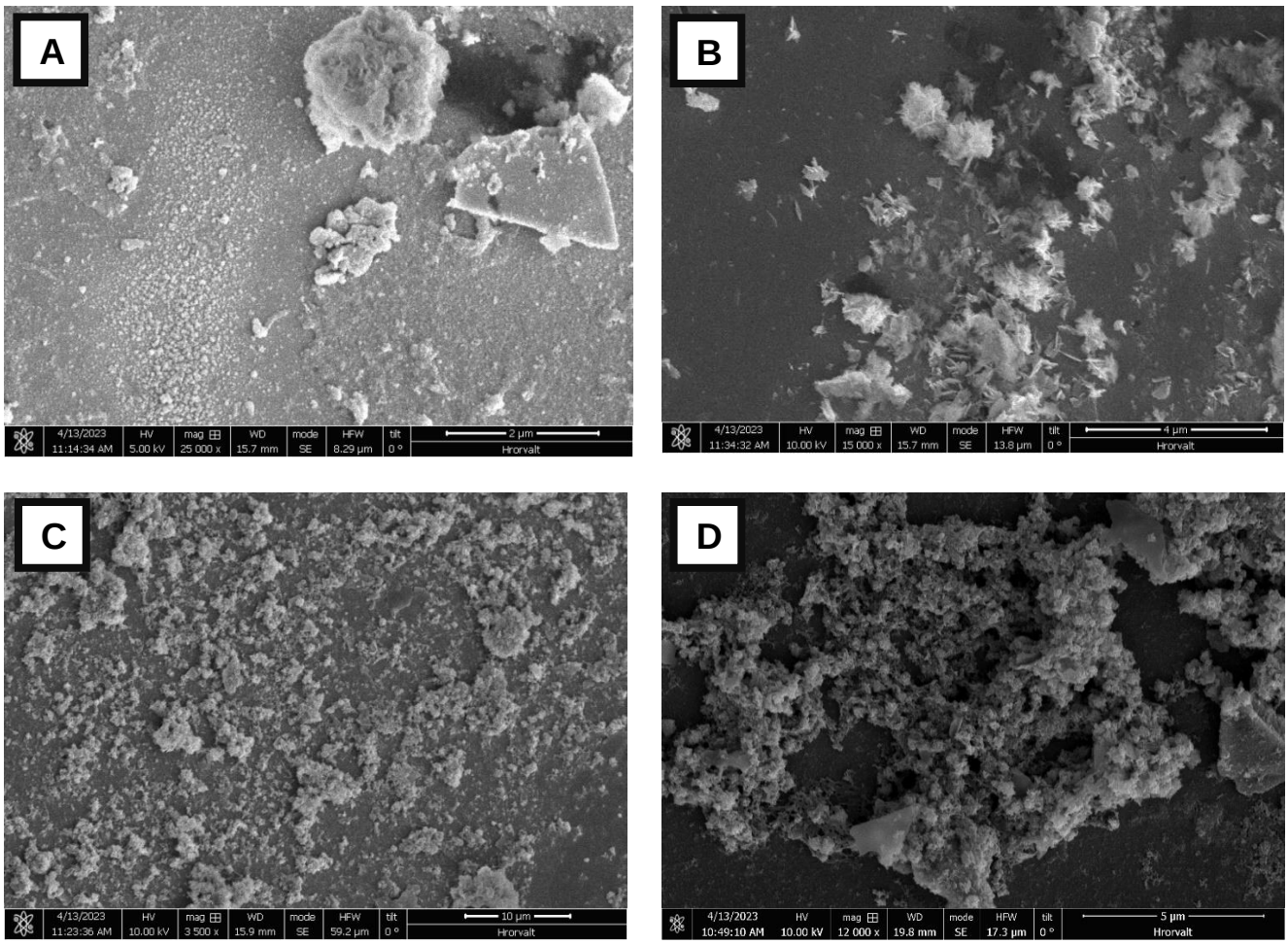

Figure 3-11 SEM images of polished pyrite cubes recovered after the experiments. SEM-EDX analysis of these images are provided in Appendix A (p. 45)

4 Discussion

This thesis aimed to investigate the processes involved in anoxic iron removal from groundwater using sulfide addition in an up-flow column reactor filled with pyrite seeding crystals. This chapter starts with determining whether pyrite had formed and discusses the possible mechanisms which influenced pyrite formation under the applied experimental conditions (4.1). Section 4.2 elaborates on what iron sulfides and products besides pyrite formed. Continuing with a discussion on where iron sulfides formed and how they were retained in the pyrite filled up-flow column reactor (4.3). Considerations regarding the molar removed iron to removed sulfide ratio observed in the dose response iron sulfide formation test are presented in section 4.4. Finally, section 4.5 aims to address the relevance of the results for groundwater treatment applications.

4.1 Feasibility & Mechanisms of Pyrite Formation under Investigated Experimental Conditions

The aim of this section is to discuss whether pyrite had formed and to elaborate on the possible mechanisms which influenced pyrite formation under the applied experimental conditions. It therefore addresses the first research sub-question (1.3). The findings suggest minor amounts of pyrite formed. No crystal growth occurred, and the formation pathway was likely via the H_2S pathway resulting from a secondary nucleation.

In this study three analytical techniques were employed that allow to identify pyrite formation. Firstly, pyrite was not detected by XRD-analysis. Secondly, one out of 15 analyzed locations showed a Raman pattern indicating the presence of pyrite. Lastly, no indications of pyrite crystal growth or deposition of nucleated pyrite crystals could be detected by SEM observations.

The assumed formation mechanisms are derived from literature. Figure 4-1 provides an overview of the formation pathways leading to pyrite formation, which are relevant to the employed experimental set-up.

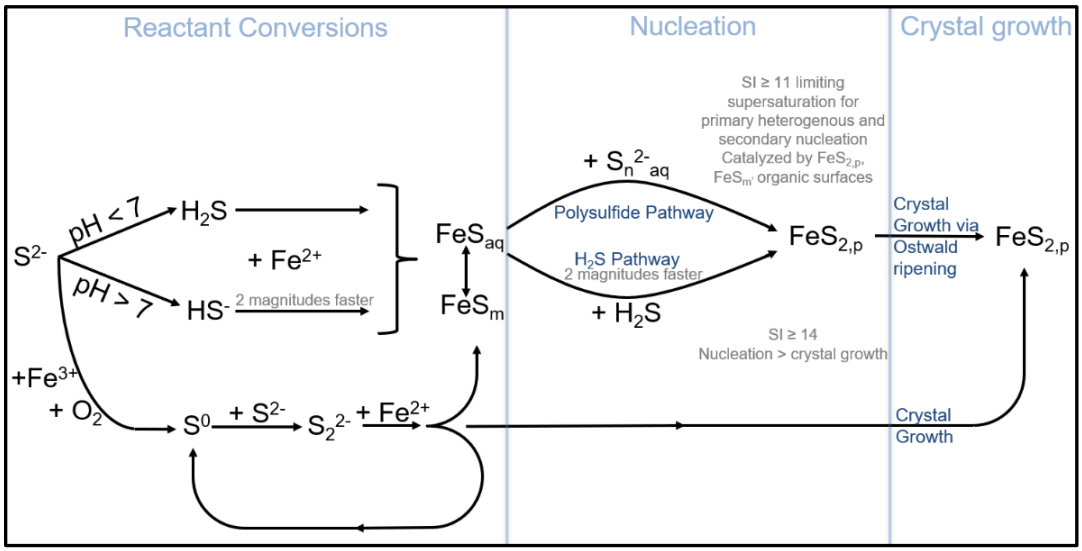

Figure 4-1 Reaction pathways for pyrite formation and its reactants at ambient conditions [20], [21], [37], [40]–[42], [53]–[55]

This section is divided in five parts. First, the results relevant for pyrite identification are interpreted. From there, it continues by discussing possible pyrite formation pathways with respect to the investigated experimental conditions, followed by an elaboration on competing mechanisms which likely hindered pyrite formation. Fourthly, a brief design recommendation is given for a chemostat reactor which could lead to pure pyrite formation via crystal growth. The section finishes by summarizing the key-messages.

Interpretation of Pyrite Identifying Analysis

This section interprets the employed analysis for pyrite identification. Only minor amounts of pyrite formed during the reactor operation. Pyrite was solely detected by Raman analysis (Figure 3-7).

The pyrite detected by Raman spectroscopy could originate from either formation or flushed out pre-existing crystals. However, seeding crystals were significantly bigger (⌀ > 1.4 mm) than the observed solids retained on the filter and hydrodynamic conditions are not considered to cause a break off and subsequent flush out of micro-scale pyrite particles. Therefore, it is assumed that pyrite formed in the column.

Pyrite was not identified by XRD measurements. Commonly, XRD is considered as the main method for pyrite identification [20]. Most likely, this is related to the minor fraction that pyrite represented.

Pyrite Formation Mechanisms

There are three mechanisms leading to pyrite formation relevant for this investigation (Figure 4-1). These can be categorized in nucleation and crystal growth [21]. Nucleation can occur via the polysulfide [21], [37], [53], [56] and H_2S pathway [21], [37], [39], [40], crystal growth via the congruent dissolution reaction (Figure 4-1, bottom) [21]. These pathways are discussed with respect to the experimental conditions. All these pathway are thermodynamically favorable at investigated conditions [20].

Firstly, the polysulfide pathway did not occur under investigated experimental conditions. The pH during the experiments was ca. 6.0 ± 0.2. Polysulfides only make up a minor fraction at this pH [57]. This fraction is not sufficient to reach supersaturations required for nucleation. For instance, at the pH of 6 and a concentration of 10mg S^{2-}/L, >9.9 mg/L is present as H_2S and only 1µg/L as HS_2^-, the most dominant polysulfide species at this pH. Furthermore, the polysulfide pathway is ca. two magnitudes slower than the H_2S pathway [37]. It is therefore considered that it did not contribute to the anyway small amount of detected pyrite.

Secondly, no crystal growth was detected under employed experimental conditions. Crystal growth could have occurred via reaction of HS_2^- and Fe^{2+}. Based on theoretical considerations it is argued that only picomolar HS_2^- are necessary in the presence of nanomolar dissolved iron to form FeS_{2p} [20]. This demonstrates that, hypothetically there was sufficient HS_2^- accounting for pyrite formation. However, it is assumed that the formation of FeS_m hindered crystal growth. FeS_m forms rapidly under experimental conditions similar to this study [21]. It is observed that "*pyrite crystals grow quite readily in environments where reactants like FeS_m are not present and the growth mechanism is likely to be a more direct process*" [21]. Thus, rapidly forming FeS_m has hindered crystal growth by taking up reactants and potentially by covering the seeding crystals surface. This is elaborated in the following section on competing mechanisms for pyrite formation.

Lastly, it is concluded that the H_2S pathway caused pyrite formation via secondary nucleation. First, since the other two possible pathways are excluded and secondly since the theoretic requirements are fulfilled. H_2S and Fe^{2+} are present in sufficient concentrations for the SI to exceed 11 (p.55) and pyrite seeding crystals are present to catalyze this reaction [42].

Competing Mechanisms for Pyrite Formation

This section discusses competing mechanism that hindered pyrite formation. It is assumed, that pyrite formation kinetics were retarded by FeS_m formation, resulting in little to no pyrite formation observed in this study.

Firstly, it should be noted that the product of pyrite formation experiments rarely is 100 wt% pyrite [20]. This is for instance due to co-occurring competing FeS_m formation [20]. Therefore, a mix of iron sulfides and other reactants will always be present [20]. However, this does not explain the low formation of pyrite.

The surface catalytic effects of pyrite seeding crystals were too low and previously formed FeS_m depleted reactants and blocked crystal growth. As the SI decreases nucleation becomes less dominant and solely crystal growth takes over. FeS_m forms more rapidly than pyrite [21] under the studied experimental conditions. Thus, previously formed FeS_m could have simply depleted the reactants and blocked the surface of the seeding crystals, preventing crystal growth.

However, it should be noted, that pyrite is the stable phase in this system. Meaning, in an infinite time scenario, FeS_m would constantly dissolve in the presence of pyrite, providing the reactants for pyrite crystal growth. This is due to the higher solubility of FeS_m compared to pyrite [21]. The concentrations of Fe^{2+} and S^{2-} in solution with respect to the equilibrium concentration of FeS_m are sufficient to allow for pyrite crystal growth, due to the extreme low solubility of pyrite. Meaning FeS_m formation leads to a retardation of pyrite formation since it introduces an intermediate step. This probably accounts for the observation that barely any pyrite formed within the 19min HRT applied in this investigation. Although, kinetic rates from other studies suggested the general feasibility of tested timescales [37]–[39] (1.2).

Another reason for minor pyrite formation might be the lower sulfide to iron dosing ratio compared to other pyrite formation studies. Most experimental studies aiming for pyrite formation applied a sulfide overdose with respect to the molar Fe:S ratio of 1:2 in pyrite [41], [58]. However, this study utilized a maximum ratio of 1:2 and the actual measured ratio was a maximum of ca. 1:1.5, due to the extreme sensitivity of <1mM sulfide solutions to oxidation [21].

Design Recommendation: Pyrite Crystallization Chemostat Reactor

This section gives a design recommendation for a pyrite forming chemostat reactor aiming for crystal growth and no by-product formation. The advantage of pyrite over other iron sulfides is its high stability over a wide range of conditions [36]. The stability allows for easy storage and its utilization in non-in-situ applications.

A chemostat is continuously fed while ionic concentrations are kept constant. The concentration of sulfide and iron would be maintained below the saturation limit of FeS_m which equal 0.4mg S^{2-}/L and 2.1 mg Fe^{2+}/L at a pH of 6 (similar to p. 54). The feeding rate is determined by the incoming Fe^{2+} concentration and the crystal growth rate. The advantage of this system is the avoidance of FeS_m formation which is likely retarding pyrite formation [21]. Additionally, the required supersaturations needed are lower since crystal growth is aimed for (SI>11 for nucleation). Sulfide could be dosed as polysulfide, to allow for sufficient S_2^{2-}, which is needed for the crystal growth mechanism [21]. The relative low equilibrium concentration of S_2^{2-} should not hinder pyrite formation, since only picomolar HS_2^- are required for pyrite formation [20] and polysulfide distributions equilibrate rapidly [59]. A pH of 6 seems to allow for highest possible FeS_m solubility while preventing marcasite formation [21].

There are three main considerations regarding such a system. Firstly, it would be crucial to have a thorough initial mixing, to avoid local supersaturations provoking FeS_m formation. This applies for both the incoming iron media (e.g., groundwater) and the sulfide solution. Secondly, it is important

to keep such a system strictly anoxic due to the low concentrations of sulfide, which is easily oxidized [21]. Lastly, pyrite seeding crystals should be in suspension to allow for good mixing and a high active surface area. Obviously, the pyrite seeding crystals should be retained in the chemostat. An earlier study can provide guidance for such a design. There, they described the application of a fluidized bed reactor for in-situ electrochemical generation of H_2S with a precision of ±0.25% in concentration ranges of 0.06 and 1900 µmol L^{-1}[60].

Summary: Minor Amounts of Pyrite Formed via H_2S-pathway

This section has reviewed whether pyrite had formed and elaborated on possible mechanisms which influenced pyrite formation. In sum, it is concluded that pyrite formed via the H_2S pathway through secondary nucleation. However, it has only made up a minor fraction of formed solids. FeS_m formation retarded pyrite formation by taking up reactants, blocking pyrite seeding crystals and therefore introducing intermediate reaction steps towards pyrite formation. Crystal growth was consequently mitigated. Lastly, a chemostat reactor operating at concentrations below the supersaturating limit of FeS_m is proposed for pure pyrite crystal growth.

4.2 Formation of Iron Sulfides & Products Besides Pyrite

The aim of this section is to discuss what iron sulfides and products besides pyrite formed under investigated experimental conditions. It therefore addresses the second research sub-question (1.3). The findings suggest that mackinawite and rhombic sulfur formed. Moreover, lepidocrocite was identified in an oxidized effluent sample. The formation of greigite (Fe_3S_4) and marcasite ($FeS_{2,ma}$) can almost certainly be excluded.

Within this research rhombic sulfur(S_8) was identified by Raman spectroscopy (Figure 3-7). The presence of FeS_m was detected by SEM pictures (Figure 3-9) and visual inspections (p. 43) complemented by literature investigations. Lepidocrocite was identified in an oxidized effluent sample (p. 42). SEM-EDX analysis revealed an Fe:S ratio on the pyrite crystals surface of 1:4.5 ± 0.6 (3.4.4).

This section is categorized in six parts. First, the formation of mackinawite is discussed. Secondly, Fe(III) formation and Fe(II) release during the stabilization tests (3.1) are explained. Afterwards, formation mechanisms are reviewed which led to the high presence of identified rhombic sulfur (S^0). The section continues by evaluating the anoxic conditions during reactor operation and further addresses the likelihood of greigite (Fe_3S_4) and marcasite ($FeS_{2,ma}$) formation. Lastly, the key-messages are summarized.

Mackinawite Formation

The main solid that formed in this investigation was mackinawite. Although, the proof of FeS_m formation by analytical methods employed in this study is weak, FeS_m formation becomes apparent when comparing investigated conditions to similar experiments in literature.

Mackinawite is usually the first precipitate to form in anoxic iron sulfide experiments at ambient temperatures [21], [61]. It has been observed in many studies approaching pyrite formation [20] due to its rapid formation kinetics and low solubility [62].

FeS_m forms from the reaction of HS^-, HS_2 and polysulfides with Fe(II) and becomes visible in solutions as black nanoparticulates (3-7nm) [55]. In this study, the sampled influent clearly showed a black discoloration (p. 43).

Furthermore, the rate equation applied to the investigated conditions of 20 mg Fe^{2+}/L and 11.5 mg S^{2-}/L for FeS_m formation yields initial formation rates that suggest a depletion of reactants

in approximately 6.6 minutes. This is a third of the applied HRT and matched well with the observation that most of the black precipitates retained in the bottom half of the up-flow-column reactor.

Lastly, the oxidation products of FeS_m, lepidocrocite and S^0 [63], were identified. Lepidocrocite was detected on oxidized effluent filter residues by XRD (Figure A-3). Rhombic sulfur (S^0) was detected on effluent filter residues by Raman spectroscopy (Figure 3-7). However, the presence of S^0 is probably caused by S^{2-} oxidation as elaborated in the section on rhombic sulfur formation.

There are two reasons why mackinawite was barely detected in this study, though its formation seems so apparent. Firstly, the nanoparticulate FeS_m is sensitive to oxidation [20], [64], [65]. Even though handled carefully, it cannot be excluded that FeS_m oxidized before analysis. Secondly, the nanoparticulate crystal size is too small to be detected by XRD [20]. XRD therefore indicates it is an amorphous state, although it is not [66]. Mössbauer spectroscopy seems to overcome the issues of the nanoparticulate size, since it *"does not require long-range ordering of the crystal structure"* [64].

Fe(III) Formation & Fe(II) Release by Sulfide Oxidation During the Concentration Stabilization Tests

This section discusses the mechanisms that led to Fe(III) retention and Fe(II) release observed during the iron and iron sulfide stabilization test, respectively (Figure 3-2, Figure 3-3). Fe(III) formed by oxidation via O_2. These Fe(III) hydroxides were reduced by oxidation of sulfide to rhombic sulfur during the iron sulfide stabilization test. After consumption of Fe(III) hydroxides, sulfide reacted with the incoming Fe^{2+} to from FeS_m.

It is assumed that Fe(III) hydroxides accumulated in the up-flow column reactor during the iron stabilization test (Figure 3-2). These almost certainly originated from the oxygen which was detected in the influent (3.1.2). Once the sulfide was dosed, it preferably reacted with the Fe(III) hydroxides compared to the dosed Fe(II). This matches with results from an earlier study, where it was identified that sulfide reacts faster with Fe(III) than Fe(II) [16]. Fe(III) was reduced and therefore released Fe(II) in solution. This explains the increased Fe(II) effluent concentrations after sulfide dose was started (Figure 3-3). Interestingly, the same phenomenon is observed in sediments, where dissolved sulfide reacts with Fe(III) hydroxides releasing Fe(II) [67]. After consumption of Fe(III)-hydroxides the sulfide reacted with Fe(II) forming FeS_m, as discussed above.

Rhombic Sulfur Formation

This section addresses the rhombic sulfur formation. Rhombic sulfur likely formed through the oxidation of sulfide by oxygen and was detected by Raman spectroscopy in the effluent samples (Figure 3-7). Other pathways for rhombic sulfur formation are via the instability of S^{2-} at investigated Eh, pH conditions, oxidation of the used sulfide source in storage location or via sulfide oxidation by the presence of Fe^{3+}.

Approximately, on average half of the dosed sulfide was detected in the reactor influent. The intended sulfide doses were 11.5 and 23 mg S^{2-}/L, respectively (Table 2-1). However, the measured concentrations were significantly lower equaling 5.3 ±1.7 and 11.7 ±2.6 mg S^{2-}/L, respectively. (Figure 3-4).

There are four mechanism which could have caused rhombic sulfur (S^0) formation. Firstly, and most probably this difference is caused via oxidation by oxygen, as sulfide solutions at millimolar concentrations are sensitive to this process [21]. Oxygen might have been introduced during media preparation and via the tubes. Secondly, it is assumed that some S^{2-} reacted to rhombic sulfur not caused by O_2-oxidation. The is due to the instability of S^{2-} at investigated Eh, pH conditions [61] as

shown in the Pourbaix-diagram ((Figure D-1). At the investigated pH of approximately 6.0 ± 0.1, rhombic sulfur can form. Thirdly, atmospheric storage of $Na_2S \cdot 9H_2O$ salt can lead to S^{2-} oxidation, resulting in lower-than-expected dosed S^{2-} concentrations [45]. Lastly, Fe^{3+} in the incoming iron solution can cause sulfide oxidation by iron reduction causing the formation of Fe^{2+} and rhombic sulfur [16], [21]. As a side remark, the Pourbaix diagram (Figure D-1) may also explain why no rhombic sulfur formed during the sulfide stabilization test. The pH during this test was 6.9. The rhombic sulfur stability range is nearly exceeded at this pH.

Anoxic Conditions During Reactor Operation

Small oxygen contaminations were detected. However, it is assumed that the small incoming oxygen contaminations rapidly depleted and therefore had negligible effects on the overall experiments. The three possible mechanisms leading to oxygen depletion are reduction by S^{2-}, Fe^{2+} or SO_3^{2-}. These mechanisms are discussed with respect to the results of the sulfide stabilization (3.1.1) and iron stabilization test (3.1.2).

Iron oxidation is faster than SO_3^{2-} oxidation, otherwise no iron would have been oxidized during the iron stabilization test (Figure 3-2). Sulfide oxidation as oxygen depleting mechanism is uncertain in this investigation. Sulfide either reacted with oxygen before entering the reactor or oxygen reduction via sulfite was faster. This is evident because the sulfide concentration in the effluent matched that of the influent in the sulfide stabilization test (3.1.1). A theoretical incoming O_2 concentration of 0.33mg O_2/L[2] would have caused a 1.3 mg S^{2-}/L off-set.

Fe(III) hydroxides are rapidly reduced by sulfide [16]. This means, that sulfide was ultimately oxidized either way: Directly or via the reduction of Fe(III) to Fe(II) and Fe(II) concentrations eventually stayed unaffected. Hence, Fe(II) was not removed via oxidation.

Absence of Greigite and Marcasite Formation

The formation of greigite (Fe_3S_4) and marcasite ($FeS_{2,ma}$) is unlikely under investigated experimental conditions. Both were not observed with any analytical techniques employed. Marcasite only forms at pH < 6 with fast reaction kinetics at a pH < 4 [20]. The pH during reactor operation was barely below 6 (3.3). It is therefore assumed that no marcasite formed. Greigite forms via its necessary precursor FeS_m according to equation (5) [68], [69]. Although, FeS_m was observed in significant quantities during this investigation, greigite formation seems thermodynamically improbable ($\Delta G^{0'}_r$ = + 14kJ) [70], [71].

$$H_2S + 3FeS_m \rightarrow Fe_3S_4 + H_2 \quad (5)$$

Summary: Dominant Formation of FeS_m and Rhombic Sulfur

This section has reviewed iron sulfides and products formation other than pyrite under investigated conditions. FeS_m formation was proven by the blackening of the influent, SEM pictures, the identification of its oxidation products, kinetic considerations and comparison of investigated conditions to relevant literature. In the iron sulfide stabilization test (3.1.3), Fe(III) hydroxides that had formed during the iron stabilization test (3.1.2) were reduced through the oxidation of S^{2-} to rhombic sulfur (S^0), resulting in the release of Fe(II) until all Fe(III) was depleted. Sulfide oxidation probably led to a rapid depletion of incoming oxygen contaminations forming rhombic sulfur. It is

[2] The 0.33 mg O_2/L are derived stoichiometrically from the average off-set of 2mg Fe/L between in- and effluent concentrations during the iron stabilization test (3.1.2).

further assumed that sulfide oxidation by Fe^{3+}, instability of sulfide at investigated Eh, pH conditions and prior oxidation of the sulfide salt due to atmospheric storage further led to sulfide depletion and rhombic sulfur formation. Greigite and marcasite formation are excluded.

4.3 Location of Iron Sulfides Formation and Retention Mechanism

The aim of this section is to discuss where iron sulfides formed and how they were retained in the pyrite filled up-flow column reactor. It therefore answers the third research sub-question (1.3). In addition to that, the observed retention of sulfur on the seeding crystals is addressed. This study suggests that FeS_m and pyrite formed in solution. Some of the FeS_m was retained, while some was flushed out. FeS_m probably retained via electrostatic adhesion to the pyrite seeding crystals. The minor fraction of formed pyrite flushed out.

This section is divided in four parts. First, it is discussed where FeS_m and pyrite formed. Secondly, the retention mechanism of FeS_m is reasoned. It continues by addressing observations of sulfur retention on the seeding crystals. Lastly, a section summary is provided.

Location of FeS_m and Pyrite Formation

There are several indications that FeS_m and pyrite formed in solution and not on the pyrite seeding crystals. Firstly, formation of FeS_m indicated by blackening of the solution was observed already when sampling the influent (p.43). Therefore, FeS_m formed independently of the pyrite seeding crystals. Secondly, it is assumed that the minor fraction of pyrite also formed in solution, since no pyrite crystal growth could be observed, as discussed above in section 4.1. However, it seems that pyrite formation was catalyzed by the pyrite seeding crystals surface.

FeS_m Retention via Electrostatic Adhesion

This section discusses the retention mechanisms of FeS_m in the up-flow column reactor. It is hypothesized that FeS_m was retained by electrostatic adhesion on pyrite seeding crystals.

This mechanism is illustrated by comparing the point of zero charges (PZC) for FeS_m and pyrite with the pH during the experiments. The PZC of mackinawite equals pH = 7.5 [55]. Meaning the FeS_m surface is charged positively at a pH < 7.5 and negatively at a pH > 7.5. The PZC of pyrite is pH 2 in the absence of potential-determining ions (PDI) and pH 5 in the presence of PDI, specifically around 28 mg Fe^{2+}/L [72]. This implies that, at the measured pH of approximately 6 ± 0.1, the pyrite surface is negatively charged, while the FeS_m surface is positively charged. The opposite surface charges probably led to the retention of FeS_m on the pyrite seeding crystals surface.

Retention based on density and size can almost certainly be excluded. In order for the settling velocity of FeS_m particles to become larger than the up flow velocity in the column, the required minimum particle size would need to be approximately 15µm (assuming a density of FeS_m = 4.4g/cm³ [73]). However, FeS_m formed under this conditions is usually nanoparticulate and therefore 3-4 magnitudes smaller [55]. Moreover, it has been proven unsuccessful to form mackinawite crystals >10µm [65].

However, the previous considerations are neglecting wall effects. The diameter of the column (19mm) was only ca. nine times bigger than the average pyrite crystal size (2.1mm). Wall effects in the investigated system might have led to substantially faster flow rates at the wall compared to the crystal bed. Overall, this might have caused lower HRT and complicates size and density-based removal mechanisms. Nonetheless, particle size-based retention in the pore space can almost certainly be excluded due to the nanoparticulate size of FeS_m.

Sulfur Retention on Pyrite Seeding Crystals

The SEM-EDX analysis of the pyrite seeding crystals surface revealed an average Fe:S ratio of 1:4.5 ± 0.6. This matches well with the average retained sulfide concentrations throughout the experiments which equaled roughly 1:4.5. The retained sulfide concentration was estimated by subtracting the measured effluent concentration (Figure 3-4) from the intended dose (Table 2-1). In comparison, pyrite would yield an Fe:S ratio of approximately 1:2 according to SEM-EDX [74]. This indicates sulfur accumulation on the pyrite crystal surface.

The relatively high sulfur fraction is likely derived from the oxidation of sulfides to rhombic sulfur (S^0). Rhombic sulfur forming mechanisms are elaborated on the previous section (4.2). It is improbable that sulfate would retain on the pyrite seeding crystals since both the crystals and sulfate are negatively charged at a pH of approximately 6, suggesting repulsion between them. Additionally, no sulfate sorption is expected on FeS_m [75]. A similar behavior is assumed for sulfite. Polysulfides are rather unstable at this pH and therefore are not expected to account for the adhered sulfur [57].

Summary: FeS_m Formation in Solution & Retention via Electrostatic Adhesion

In summary, it is concluded that pyrite was formed in solution as no crystal growth was observed. Similarly, FeS_m formed in solution since the influent turned black before getting in contact with the seeding crystals. It is further concluded that FeS_m retained on the pyrite seeding crystals due to electrostatic adhesion at the investigated pH. Density and size-based retention mechanisms are ruled out. The formed pyrite flushed out and lastly, the relatively high Fe:S ratio observed with SEM-EDX was likely caused by retained rhombic sulfur.

4.4 Considerations on Removed Iron to Removed Sulfide Ratio

This section discusses the ratio of removed iron to sulfide observed in the dose response iron sulfides formation test. It therefore addresses the fourth research sub-question (1.3). This study obtained a Fe_{rem}:S^{2-}_{rem} ratio of approximately 0.4 ± 0.2 (1:2.5) and 0.8 ± 0.2 (1:1.25), for molar dosing ratios of Fe:S^{2-} = 1:1 and 1.2, respectively (3.3). Further relevant results with respect to these ratios were obtained by the solid phase analysis. XRD did not detect any iron sulfides (Figure 3-6). Raman spectroscopy identified rhombic sulfur and pyrite (Figure 3-7). SEM-EDX did not identify pyrite crystal growth but revealed the presence of adhered FeS_m and a Fe:S ratio on the pyrite crystals surface of 1:4.5 ± 0.6 (3.4.4).

This section is divided in five parts. It starts by discussing the influence of the high uncertainty and the effluent S^{2-} quantification method. Next, it expands on the theoretical maximum Fe_{rem}:S^{2-}_{rem} ratio (1:1) and continues by providing explanations why the ratios were below 1. Reasonings are provided, why the Fe_{rem}:S^{2-}_{rem} ratio was lower for the lower sulfide dose (Fe:S^{2-} = 1:1) compared to the higher dose (Fe:S^{2-} = 1:2). Lastly, a section summary is provided.

Considerations Regarding the High Uncertainty & Effluent S^{2-} Quantification

There are two general considerations regarding this section (4.4) on the Fe_{rem}:S^{2-}_{rem} ratio: (i) the high uncertainty of quantified values and (ii) the effluent S^{2-} quantification. Firstly, the observed uncertainty ranges are high. Expressed in relative standard deviations, these equal 0.4 ± 50% and 0.8 ± 25%. Therefore, interpretations must be made cautiously. More datapoints obtained from a longer run time could provide a clearer picture. Secondly, it is assumed that most of the effluent sulfide is FeS_m bound sulfide. Similarly to other studies [76], the S^{2-} quantification method could not differentiate between S^{2-} and FeS_m bound sulfide (p. 48). Furthermore, kinetic considerations of FeS_m formation indicate consumption of all reactants until equilibrium (4.2). The equilibrium

concentrations at an observed pH of 6.1 equal 0.3 mg S^{2-}/L and 1.9mg Fe^{2+}/L (estim. with Phreeqc p. 54). Since effluent S^{2-} concentrations were usually >1mgS^{2-}/L, this means, that the obtained Fe_{rem}:S^{2-}_{rem} ratios are slightly underestimating the actual ratios of formed iron sulfides.

The Highest Possible Fe_{rem}:S^{2-}_{rem} Ratio Equals 1:1

The highest possible Fe_{rem}:S^{2-}_{rem} ratio equals 1:1. This is based on two considerations. Firstly, there is no iron sulfide mineral which has a higher ratio of Fe:S = 1:1 (Table D-1). Secondly, it is assumed that there is no competing mechanism leading to iron retention other than the iron sulfides formation. This is presumed since the iron stabilization test revealed stable conditions after ca. 110 pore volumes. Meaning, there is no further adsorption expected. Moreover, Fe(III) hydroxides accumulation can be excluded since incoming sulfides are readily reducing them releasing Fe^{2+} in solution[16]. It is assumed that pyrite seeding crystals were saturated with Fe^{2+}, due to the stabilization phase (3.1.3) before estimating the molar ratios (Figure 3-5). Furthermore, no sorption of Fe^{2+} to FeS_m and rhombic sulfur is expected due to their positive and neutral charge, respectively [55].

Causes for Fe_{rem}:S^{2-}_{rem} < 1

This section elaborates on possible explanations why the Fe_{rem}:S^{2-}_{rem} ratios were below one. Iron sulfides formation and S^{2-} consuming side reactions are considered.

Firstly, the ratios Fe_{rem}:S^{2-}_{rem} < 1 are unlikely to be accounted for by the formation of iron sulfides of $FeS_{x>1}$ (e.g., pyrite, greigite & marcasite). The only $FeS_{x>1}$ which was detected is pyrite and only represented a minor fraction (as discussed in 4.1). Moreover, the formation of greigite and marcasite is highly unlikely under investigated conditions (4.2). Therefore, other reactions must have led to observed ratios <1. Secondly, it is probable that S^{2-} consuming side reactions caused this offset. For instance, sulfide reacting to rhombic sulfur as elaborated in section 4.2.

Difference Between Fe_{rem}:S^{2-}_{rem} Ratios for Both Fe:S^{2-} Dosing Ratios

However, the observed Fe_{rem}:S^{2-}_{rem} ratios are not only lower than 1. The lower dosing ratio of Fe:S^{2-} = 1:1 resulted in half the Fe_{rem}:S^{2-}_{rem} ratio compared to the higher dosing ratio of 1:2, equaling 0.4 ±0.2 and 0.8 ± 0.2, respectively. There are two mechanisms that could explain this.

Firstly, the Fe^{3+} potentially contained in the influent would lead to the same absolute amount of sulfide reduction for both dosing ratios. However, since the absolute dosing ratios differed, the relative fraction is bigger for the lower dose, ultimately leading to a lower Fe_{rem}:S^{2-}_{rem} ratio for the lower dose compared to the higher dose. Secondly, a higher sulfide concentration lowers the redox potential (Figure E-1). Looking at the Pourbaix diagram for sulfur (Figure D-1), this shifts the conditions away from stable regions of rhombic sulfur. This means less sulfide reacts to rhombic sulfur at the higher dose and is therefore available for reacting with Fe^{2+} ultimately leading to a higher Fe_{rem}:S^{2-}_{rem} ratio.

Summary: The Fe_{rem}:S^{2-}_{rem} Ratio Equaled up to 0.8 ± 0.2

This section discussed the removed iron to removed sulfide ratios (Fe_{rem}:S^{2-}_{rem}) for the dosing ratios of Fe:S^{2-} = 1:1 and 1.2, which equaled approximately 0.4 ± 0.2 (1:2.5) and 0.8 ± 0.2 (1:1.25), respectively. The relative uncertainties of the ratios are high. It is assumed that a large fraction of effluent sulfide is FeS_m bound. Moreover, the highest possible Fe_{rem}:S^{2-}_{rem} ratio equals 1:1. Deviations from this ratio a probably not caused by Fe:$S_{x>1}$ iron sulfides formation. It seems that, rhombic sulfur formation via various pathways (4.2) led to S^{2-} consumption. Lastly, it is suggested

that the Fe_{rem}:S^{2-}_{rem} ratio for the lower sulfide dose was smaller due to the higher influence of the possible Fe^{3+} contamination and the different redox potentials at each dosing ratio.

4.5 Iron Sulfides Formation for Groundwater Treatment

The aim of this section is to briefly discuss the relevance of the results for groundwater treatment applications. This study showed rapid anoxic FeS_m formation in solution upon sulfide dose and achieved molar Fe_{rem}:S^{2-}_{rem} of up to 0.8 ± 0.2.

Experimentally observed FeS_m formation characteristics indicated general applicability for typical groundwater treatment settings for two reasons. Firstly, FeS_m forms rapidly within a timeframe of a few minutes which allow for small reactor design. Secondly, FeS_m particles can be removed electrostatically, due to their charge. In combination with their nanoparticulate size, this could lead to simple removal via an oppositely charged surface. For instance, an electrically charged surface, which allows for charge dependent adhesion and detachment.

In-situ electrochemical sulfate reduction producing S^{2-} could provide a viable solution for iron sulfides formation. With this approach, groundwater native sulfate is reduced electrochemically to S^{2-} [33], [34], so there is no need for chemical sulfide dosage. The estimated costs for electrochemical generation of sulfide to treat a groundwater containing 10mg Fe^{2+}/L equal 0.012€/m³ and 0.025 €/m³, for the formation of mackinawite and pyrite, respectively (Appendix F). These costs could be covered by the sale of produced iron sulfides and by reduced RSF-backwash frequencies and backwash water treatment. While, the principle feasibility of in-situ electrochemical sulfate reduction producing S^2 has been demonstrated [33], [34], [60], further investigation is required for its application using groundwater.

The rapidly formed iron sulfides, particularly mackinawite, are not only removing iron, but have several properties, that allow to be employed for further treatment of water. FeS_m can be used for the simultaneous treatment of As(III). The adsorption capacity of As(III) to FeS_m was estimated to equal 0.012 mol As(III) per mol FeS_m [77]. Converting this to Fe^{2+} equals a capacity of 16 µg As(III)/mg Fe(II). Next to adsorption, there are a few more pathways for As removal in iron sulfides system which were reviewed recently [23]. These include the formation of minerals such as orpiment (As_2S_3) and realgar (AsS) or the removal via precipitation as AsFe-S minerals such as arsenopyrite (FeAsS)[23].

Another study reviewed the potentials of iron sulfide for waste water treatment [24]. They identified four groups of target pollutants, which can be treated: (i) toxic metals and metalloids [65], (ii) radionuclides, (iii) organic contaminants and (iv) nutrients such as nitrogen and phosphor [78]. This is illustrated by specific studies which investigated applications of FeS and MnS as an electron donor for denitrification and chromium reduction [79] or studies which used FeS as an activator for enhancing PFOA [80] and pharmaceuticals removal [81].

All in all, sulfide dose has the potential for iron removal via iron sulfides formation which can be used for further treatment of potential GW contaminants. Moreover, sulfide can be dosed in-situ via electro-chemical reduction of GW native sulfate.

5 Conclusion & Recommendations

This thesis aimed to explore the novel concept of anoxic iron removal in GW treatment via iron sulfides formation and to identify the involved processes. To investigate this, an up-flow column reactor filled with pyrite seeding crystals was built and fed with iron and sulfide containing solutions.

Iron can be removed from a (synthetic) groundwater solution by rapid mackinawite (FeS_m) formation. Separation of nanoparticulate FeS_m particles can be achieved via electrostatic adhesion, in this case the negatively charged pyrite seeding crystals. The required sulfide dose for FeS_m formation was indicated by the molar ratio of removed iron to sulfide which equaled up to 0.8 ± 0.2 (1.4 ± 0.4 mg Fe/ (mg S^{2-})). Pyrite formation played a minor role under investigated conditions.

Iron sulfides formation, specifically FeS_m formation can present an interesting alternative to conventional iron removal, due to its fast formation rates, possibly simple removal mechanisms via electrostatic adhesion and its compact size. Furthermore, in-situ formed FeS_m has the potential to simultaneously treat a wide range of pollutants. These range from toxic metals and metalloids such as arsenic over organic contaminants and nutrients such as nitrate and phosphate.

The generalizability of these results is subject to certain limitations. For instance, wall effects which led to uncertain hydraulic retention times and flow behavior in the column. Furthermore, it could not be differentiated between FeS_m bound and unbound Fe^{2+} and S^{2-} and only two Fe:S^{2-} ratios were investigated. Precise FeS_m formation kinetics are therefore still uncertain.

Six recommendations are given for further research:

1. Investigate FeS_m formation in the absence of seeding crystals at different HRT and Fe^{2+} concentrations.
2. Apply an analytical method which differentiates between FeS_m bound and unbound Fe^{2+} and S^{2-} under groundwater treatment like conditions.
3. Investigate the feasibility of in-situ electrochemical S^{2-} generation by sulfate reduction using groundwater.
4. Investigate the potential of simultaneous anoxic iron and arsenic removal via sulfide dose.
5. Investigate the electrostatic adhesion and detachment behavior of in-situ formed FeS_m via an electrically charged surface.
6. If pyrite formation is intended: Investigate the concept of a chemostat reactor operating below the supersaturation limit of FeS_m for pure pyrite crystal growth.

This thesis presented the first ever application of iron removal via sulfides formation in a GW treatment context. A novel approach which has the potential to enhance the sustainability of treating the most commonly used drinking water source.

REFERENCES

[1] P. Sampat, *Deep trouble : the hidden threat of groundwater pollution*. in Worldwatch paper ; 154. Worldwatch Institute, 2000.

[2] T. Ahmad, K. Ahmad, and M. Alam, 'Sustainable management of water treatment sludge through 3"R" concept', *J. Clean. Prod.*, vol. 124, pp. 1–13, Jun. 2016, doi: 10.1016/j.jclepro.2016.02.073.

[3] R. Albrektienė, K. Karaliūnas, and K. Bazienė, 'Sustainable Reuse of Groundwater Treatment Iron Sludge for Organic Matter Removal from River Neris Water', *Sustainability*, vol. 11, no. 3, Art. no. 3, Jan. 2019, doi: 10.3390/su11030639.

[4] A. O. Babatunde and Y. Q. Zhao, 'Constructive Approaches Toward Water Treatment Works Sludge Management: An International Review of Beneficial Reuses', *Crit. Rev. Environ. Sci. Technol.*, vol. 37, no. 2, pp. 129–164, Jan. 2007, doi: 10.1080/10643380600776239.

[5] M. Mastrocicco, B. m. s. Giambastiani, and N. Colombani, 'Ammonium occurrence in a salinized lowland coastal aquifer (Ferrara, Italy)', *Hydrol. Process.*, vol. 27, no. 24, pp. 3495–3501, 2013, doi: 10.1002/hyp.9467.

[6] C. O'Sullivan, W. Clarke, and D. Lockington, 'Sources of Hydrogen Sulfide in Groundwater on Reclaimed Land', *J. Environ. Eng.*, vol. 131, no. 3, pp. 471–477, Mar. 2005, doi: 10.1061/(ASCE)0733-9372(2005)131:3(471).

[7] J. F. Barker and P. Fritz, 'The occurrence and origin of methane in some groundwater flow systems', *Can. J. Earth Sci.*, vol. 18, no. 12, pp. 1802–1816, Dec. 1981, doi: 10.1139/e81-168.

[8] N. M. Burri, R. Weatherl, C. Moeck, and M. Schirmer, 'A review of threats to groundwater quality in the anthropocene', *Sci. Total Environ.*, vol. 684, pp. 136–154, Sep. 2019, doi: 10.1016/j.scitotenv.2019.05.236.

[9] D. van Halem, 'OCW TU Delft: Drinking Water Treatment 1: Granular-filtration'. TU Delft.

[10] W. De Vet, 'Biological drinking water treatment of anaerobic groundwater in trickling filters', TU Delft, Delft, 2011.

[11] R. Goedhart, 'MSc. Thesis: Vivianite Precipitation: a Novel Concept to Remove Iron from Groundwater'. Jun. 2021.

[12] Geologische Dienst Nederland, 'Grondwaterkwaliteit in Beeld'. https://www.grondwatertools.nl/gwatlas/ (accessed Jan. 31, 2023).

[13] World Health Organization, 'Guidelines for drinking-water quality', 2011, Accessed: Jan. 31, 2023. [Online]. Available: https://apps.who.int/iris/handle/10665/44584

[14] N. Khatri, S. Tyagi, and D. Rawtani, 'Recent strategies for the removal of iron from water: A review', *J. Water Process Eng.*, vol. 19, pp. 291–304, Oct. 2017, doi: 10.1016/j.jwpe.2017.08.015.

[15] H. B. Dharmappa, A. Hasia, and P. Hagare, 'Water treatment plant residuals management', *Water Sci. Technol.*, vol. 35, no. 8, pp. 45–56, Apr. 1997, doi: 10.2166/wst.1997.0296.

[16] B. Kiilerich, A. H. Nielsen, and J. Vollertsen, 'Kinetics of sulfide precipitation with ferrous and ferric iron in wastewater', *Water Sci. Technol.*, vol. 78, no. 5, pp. 1071–1081, Aug. 2018, doi: 10.2166/wst.2018.382.

[17] E. Magnone, S. D. Kim, and J. H. Park, 'A systematic study of the iron hydroxide-based adsorbent for removal of hydrogen sulphide from biogas', *Microporous Mesoporous Mater.*, vol. 270, pp. 155–160, Nov. 2018, doi: 10.1016/j.micromeso.2018.05.018.

[18] R. Goedhart, S. Müller, M. C. M. van Loosdrecht, and D. van Halem, 'Vivianite precipitation for iron recovery from anaerobic groundwater', *Water Res.*, vol. 217, p. 118345, Jun. 2022, doi: 10.1016/j.watres.2022.118345.

[19] E. Desmidt *et al.*, 'Global Phosphorus Scarcity and Full-Scale P-Recovery Techniques: A Review', *Crit. Rev. Environ. Sci. Technol.*, vol. 45, no. 4, pp. 336–384, Feb. 2015, doi: 10.1080/10643389.2013.866531.

[20] G. W. Luther and D. Rickard, 'Chemistry of Iron Sulfides', *Chem. Rev.*, vol. 107, no. 2, pp. 514–562, 2007.

[21] D. T. Rickard, *Sulfidic sediments and sedimentary rocks*. in Developments in sedimentology, no. v. 65. Amsterdam: Elsevier, 2012.

[22] D. Rickard, 'The Many Faces of Fool's Gold', *Am. Sci.*, vol. 104, no. 3, p. 174, 2016, doi: 10.1511/2016.120.174.

[23] X. Zhang *et al.*, 'The application and mechanism of iron sulfides in arsenic removal from water and wastewater: A critical review', *J. Environ. Chem. Eng.*, vol. 10, no. 6, p. 108856, Dec. 2022, doi: 10.1016/j.jece.2022.108856.

[24] Y. Yang *et al.*, 'Utilization of iron sulfides for wastewater treatment: a critical review', *Rev. Environ. Sci. Biotechnol.*, vol. 16, no. 2, pp. 289–308, Jun. 2017, doi: 10.1007/s11157-017-9432-3.

[25] B. B. Jørgensen, 'Ecology of the bacteria of the sulphur cycle with special reference to anoxic—oxic interface environments', *Philos. Trans. R. Soc. Lond. B Biol. Sci.*, vol. 298, no. 1093, pp. 543–561, 1982, doi: https://doi.org/10.1098/rstb.1982.0096.

[26] D. Rickard, M. Mussman, and J. A. Steadman, 'Sedimentary sulfides', *Elements*, vol. 13, no. 2, Art. no. 2, 2017, doi: 10.2113/gselements.13.2.117.

[27] G. Muyzer and A. J. M. Stams, 'The ecology and biotechnology of sulphate-reducing bacteria', *Nat. Rev. Microbiol.*, vol. 6, no. 6, Art. no. 6, Jun. 2008, doi: 10.1038/nrmicro1892.

[28] I. Mendizabal, 'PUBLIC SUPPLY WELL FIELDS AS A VALUABLE GROUNDWATER QUALITY MONITORING NETWORK', Vrije Universiteit Amsterdam, Amsterdam, 2011.

[29] U.S. DEPARTMENT OF HEALTH AND HUMAN SERVICES, 'Toxicological Profile for Hydrogen Sulfide and Carbonyl Sulfide', Nov. 2016.

[30] J. E. Landmeyer, F. H. Chapelle, M. D. Petkewich, and P. M. Bradley, 'Assessment of natural attenuation of aromatic hydrocarbons in groundwater near a former manufactured-gas plant, South Carolina, USA', *Environ. Geol.*, vol. 34, no. 4, pp. 279–292, Jun. 1998, doi: 10.1007/s002540050279.

[31] A. Mukhopadhyay, A. Al-Haddad, M. Al-Otaibi, and M. Al-Senafy, 'Occurrence of hydrogen sulfide in the ground water of Kuwait', *Environ. Geol.*, vol. 52, no. 6, pp. 1151–1161, Jun. 2007, doi: 10.1007/s00254-006-0552-2.

[32] C. G. Patterson and D. D. Runnells, 'Dissolved gases in ground water as indicators of redox conditions', presented at the International symposium on water-rock interaction, 1992, pp. 517–520. Accessed: Jan. 25, 2023. [Online]. Available: http://pascal-francis.inist.fr/vibad/index.php?action=getRecordDetail&idt=6487730

[33] B. A. Bilal and H. Tributsch, 'Thermo-electrochemical reduction of sulfate to sulfide using a graphite cathode', *J. Appl. Electrochem.*, vol. 28, no. 10, pp. 1073–1081, Oct. 1998, doi: 10.1023/A:1003455219932.

[34] W. Su, L. Zhang, Y. Tao, G. Zhan, D. Li, and D. Li, 'Sulfate reduction with electrons directly derived from electrodes in bioelectrochemical systems', *Electrochem. Commun.*, vol. 22, pp. 37–40, Aug. 2012, doi: 10.1016/j.elecom.2012.04.030.

[35] M. L. McFarland and T. L. Provin, 'Hydrogen Sulfide in Drinking Water - Causes and Treatment Alternatives', p. 6, Dec. 2021.

[36] J. Ning, Y. Zheng, B. Brown, D. Young, and S. Nesic, '5507: Construction and Verification of Pourbaix Diagrams for Hydrogen Sulfide Corrosion of Mild Steel', p. 19, 2015.

[37] I. B. Butler, M. E. Böttcher, D. Rickard, and A. Oldroyd, 'Sulfur isotope partitioning during experimental formation of pyrite via the polysulfide and hydrogen sulfide pathways: implications for the interpretation of sedimentary and hydrothermal pyrite isotope records', *Earth Planet. Sci. Lett.*, vol. 228, no. 3, pp. 495–509, Dec. 2004, doi: 10.1016/j.epsl.2004.10.005.

[38] R. Guilbaud, I. B. Butler, and R. M. Ellam, 'Abiotic Pyrite Formation Produces a Large Fe Isotope Fractionation', *Science*, vol. 332, no. 6037, pp. 1548–1551, Jun. 2011, doi: 10.1126/science.1202924.

[39] D. Rickard and G. W. Luther, 'Kinetics of pyrite formation by the H2S oxidation of iron (II) monosulfide in aqueous solutions between 25 and 125°C: The mechanism', *Geochim. Cosmochim. Acta*, vol. 61, no. 1, pp. 135–147, Jan. 1997, doi: 10.1016/S0016-7037(96)00322-5.

[40] D. Rickard, 'Kinetics of pyrite formation by the H2S oxidation of iron (II) monosulfide in aqueous solutions between 25 and 125°C: The rate equation', *Geochim. Cosmochim. Acta*, vol. 61, no. 1, pp. 115–134, Jan. 1997, doi: 10.1016/S0016-7037(96)00321-3.

[41] N. G. Harmandas, E. Navarro Fernandez, and P. G. Koutsoukos, 'Crystal Growth of Pyrite in Aqueous Solutions. Inhibition by Organophosphorus Compounds', *Langmuir*, vol. 14, no. 5, pp. 1250–1255, Mar. 1998, doi: 10.1021/la970354c.

[42] I. Butler and D. Rickard, 'An anoxic chemostat for controlled sulphide mineral synthesis', no. 112, p. 2, Apr. 2003, doi: 10.1179/037174503225002045.

[43] D. Rickard, S. Grimes, I. Butler, A. Oldroyd, and K. L. Davies, 'Botanical constraints on pyrite formation', *Chem. Geol.*, vol. 236, no. 3, pp. 228–246, Jan. 2007, doi: 10.1016/j.chemgeo.2006.09.011.

[44] C. Klein, C. S. Hurlbut, and J. D. Dana, *Manual of mineralogy: after James D. Dana*, 20th ed. New York: Wiley, 1985.

[45] L. L. Bridgewater *et al.*, Eds., *Standard methods for the examination of water and wastewater*, 23rd edition. Washington, DC: American Public Health Association, 2017.

[46] R. J. Cassella1, L. G. de Oliveira1, and R. E. Santelli, 'On Line Dissolution of ZnS For Sulfide Determination in Stabilized Water Samples with Zinc Acetate, Using Spectrophotometry by Methylene Blue Method', *Spectrosc. Lett.*, vol. 32, no. 3, pp. 469–484, May 1999, doi: 10.1080/00387019909349999.

[47] 'Determination of the specific surface area of solids by gas adsorption - BET method (ISO 9277:2010)', Beuth Verlag GmbH. doi: 10.31030/2066286.

[48] D. L. Parkhurst and C. A. J. Appelo, 'Description of input and examples for PHREEQC version 3: a computer program for speciation, batch-reaction, one-dimensional transport, and

inverse geochemical calculations', U.S. Geological Survey, Reston, VA, USGS Numbered Series 6-A43, 2013. doi: 10.3133/tm6A43.

[49] C. J. Bethke, B. Farrell, and M. Sharifi, 'The Geochemist's Workbench'. Aqueos Solutions, LLC, Champaign, Illinois, USA, 2022.

[50] M. Monachon *et al.*, 'Evaluation of Bio-Based Extraction Methods by Spectroscopic Methods', *Minerals*, vol. 10, no. 2, Art. no. 2, Feb. 2020, doi: 10.3390/min10020203.

[51] S. Simon, A. Courtin-Nomade, A. Vasiliu, N. Sleiman, and V. Deluchat, 'Long-term influence of aeration on arsenic trapping in a ZVI/sand bed reactor', *RSC Adv.*, vol. 6, no. 59, pp. 54479–54485, 2016, doi: 10.1039/C6RA06565A.

[52] R. Bolney, M. Grosch, M. Winkler, J. van Slageren, W. Weigand, and C. Robl, 'Mackinawite formation from elemental iron and sulfur', *RSC Adv.*, vol. 11, no. 51, pp. 32464–32475, 2021, doi: 10.1039/D1RA03705F.

[53] G. W. Luther, 'Pyrite synthesis via polysulfide compounds', *Geochim. Cosmochim. Acta*, vol. 55, no. 10, pp. 2839–2849, Oct. 1991, doi: 10.1016/0016-7037(91)90449-F.

[54] D. E. Canfield, B. Thamdrup, and S. Fleischer, 'Isotope fractionation and sulfur metabolism by pure and enrichment cultures of elemental sulfur-disproportionating bacteria', *Limnol. Oceanogr.*, vol. 43, no. 2, pp. 253–264, 1998, doi: 10.4319/lo.1998.43.2.0253.

[55] M. Wolthers, S. J. V. D. Gaast, and D. Rickard, 'The structure of disordered mackinawite', *Am. Mineral.*, vol. 88, no. 11–12, pp. 2007–2015, Nov. 2003, doi: 10.2138/am-2003-11-1245.

[56] D. T. Rickard, 'Kinetics and mechanism of pyrite formation at low temperatures', *Am. J. Sci.*, vol. 275, no. 6, pp. 636–652, Jun. 1975, doi: 10.2475/ajs.275.6.636.

[57] A. Kamyshny, A. Goifman, J. Gun, D. Rizkov, and O. Lev, 'Equilibrium Distribution of Polysulfide Ions in Aqueous Solutions at 25 °C: A New Approach for the Study of Polysulfides' Equilibria', *Environ. Sci. Technol.*, vol. 38, no. 24, pp. 6633–6644, Dec. 2004, doi: 10.1021/es049514e.

[58] M. Wolthers, I. B. Butler, D. Rickard, and P. R. D. Mason, 'Arsenic uptake by pyrite at ambient environmental conditions: A continuous-flow experiment', in *ADVANCES IN ARSENIC RESEARCH*, American Chemical Society, 2005, pp. 60–76. Accessed: Sep. 02, 2022. [Online]. Available: https://www.research.ed.ac.uk/en/publications/arsenic-uptake-by-pyrite-at-ambient-environmental-conditions-a-co

[59] A. Kamyshny, A. Goifman, D. Rizkov, and O. Lev, 'Kinetics of Disproportionation of Inorganic Polysulfides in Undersaturated Aqueous Solutions at Environmentally Relevant Conditions', *Aquat. Geochem.*, vol. 9, no. 4, pp. 291–304, Dec. 2003, doi: 10.1023/B:AQUA.0000029023.07252.c3.

[60] S. Peiffer and W. Gade, 'Reactivity of Ferric Oxides toward H2S at Low pH', *Environ. Sci. Technol.*, vol. 41, no. 9, pp. 3159–3164, May 2007, doi: 10.1021/es062228d.

[61] D. Rickard *et al.*, 'The composition of nanoparticulate mackinawite, tetragonal iron(II) monosulfide', *Chem. Geol.*, vol. 235, no. 3, pp. 286–298, Dec. 2006, doi: 10.1016/j.chemgeo.2006.07.004.

[62] D. Rickard, 'Kinetics of FeS precipitation: Part 1. Competing reaction mechanisms', *Geochim. Cosmochim. Acta*, vol. 59, no. 21, pp. 4367–4379, Nov. 1995, doi: 10.1016/0016-7037(95)00251-T.

[63] J. He, C. J. Miller, R. Collins, D. Wang, and T. D. Waite, 'Production of a Surface-Localized Oxidant during Oxygenation of Mackinawite (FeS)', *Environ. Sci. Technol.*, vol. 54, no. 2, pp. 1167–1176, Jan. 2020, doi: 10.1021/acs.est.9b03975.

[64] C. Schröder, M. Wan, I. B. Butler, A. Tait, S. Peiffer, and C. A. McCammon, 'Identification of Mackinawite and Constraints on Its Electronic Configuration Using Mössbauer Spectroscopy', *Minerals*, vol. 10, no. 12, Art. no. 12, Dec. 2020, doi: 10.3390/min10121090.

[65] J. W. Morse and T. Arakaki, 'Adsorption and coprecipitation of divalent metals with mackinawite (FeS)', *Geochim. Cosmochim. Acta*, vol. 57, no. 15, pp. 3635–3640, Aug. 1993, doi: 10.1016/0016-7037(93)90145-M.

[66] I. B. Butler, C. Archer, D. Vance, A. Oldroyd, and D. Rickard, 'Fe isotope fractionation on FeS formation in ambient aqueous solution', *Earth Planet. Sci. Lett.*, vol. 236, no. 1, pp. 430–442, Jul. 2005, doi: 10.1016/j.epsl.2005.05.022.

[67] S. Peiffer, T. Behrends, K. Hellige, P. Larese-Casanova, M. Wan, and K. Pollok, 'Pyrite formation and mineral transformation pathways upon sulfidation of ferric hydroxides depend on mineral type and sulfide concentration', *Chem. Geol.*, vol. 400, pp. 44–55, 2015, doi: 10.1016/j.chemgeo.2015.01.023.

[68] D. Rickard and J. W. Morse, 'Acid volatile sulfide (AVS)', *Mar. Chem.*, vol. 97, no. 3, pp. 141–197, Dec. 2005, doi: 10.1016/j.marchem.2005.08.004.

[69] A. R. Lennie, S. A. T. Redfern, P. E. Champness, C. P. Stoddart, P. F. Schofield, and D. J. Vaughan, 'Transformation of mackinawite to greigite; an in situ X-ray powder diffraction and transmission electron microscope study', *Am. Mineral.*, vol. 82, no. 3–4, pp. 302–309, Apr. 1997, doi: 10.2138/am-1997-3-408.

[70] D. Rickard, I. B. Butler, and A. Oldroyd, 'A novel iron sulphide mineral switch and its implications for Earth and planetary science', *Earth Planet. Sci. Lett.*, vol. 189, no. 1, pp. 85–91, Jun. 2001, doi: 10.1016/S0012-821X(01)00352-1.

[71] J. N. Thiel, 'Pyrite Formation from FeS and H2S', Universität Konstanz, Konstanz, 2020.

[72] J. Bebié and M. A. A. Schoonen, 'Pyrite surface interaction with selected organic aqueous species under anoxic conditions', *Geochem. Trans.*, vol. 1, no. 1, p. 47, Dec. 2000, doi: 10.1186/1467-4866-1-47.

[73] H. Y. Jeong, J. H. Lee, and K. F. Hayes, 'Characterization of synthetic nanocrystalline mackinawite: crystal structure, particle size, and specific surface area', *Geochim. Cosmochim. Acta*, vol. 72, no. 2, pp. 493–505, Jan. 2008, doi: 10.1016/j.gca.2007.11.008.

[74] M. Reyes *et al.*, 'Surface Spectroscopy of Pyrite Obtained during Grinding and Its Magnetisation', *Minerals*, vol. 12, no. 11, p. 1444, Nov. 2022, doi: 10.3390/min12111444.

[75] M. Wolthers, L. Charlet, P. R. van Der Linde, D. Rickard, and C. H. van Der Weijden, 'Surface chemistry of disordered mackinawite (FeS)', *Geochim. Cosmochim. Acta*, vol. 69, no. 14, pp. 3469–3481, Jul. 2005, doi: 10.1016/j.gca.2005.01.027.

[76] P. Wilfert *et al.*, 'Sulfide induced phosphate release from iron phosphates and its potential for phosphate recovery', *Water Res.*, vol. 171, p. 115389, Mar. 2020, doi: 10.1016/j.watres.2019.115389.

[77] M. Wolthers, L. Charlet, C. H. van Der Weijden, P. R. van der Linde, and D. Rickard, 'Arsenic mobility in the ambient sulfidic environment: Sorption of arsenic(V) and arsenic(III) onto disordered mackinawite', *Geochim. Cosmochim. Acta*, vol. 69, no. 14, pp. 3483–3492, Jul. 2005, doi: 10.1016/j.gca.2005.03.003.

[78] R. Li, J. Niu, X. Zhan, and B. Liu, 'Simultaneous removal of nitrogen and phosphorus from wastewater by means of FeS-based autotrophic denitrification', *Water Sci. Technol.*, vol. 67, no. 12, pp. 2761–2767, Jun. 2013, doi: 10.2166/wst.2013.200.

[79] J. Pan, L. Liu, H. Pan, L. Yang, M. Su, and C. Wei, 'A feasibility study of metal sulfide (FeS and MnS) on simultaneous denitrification and chromate reduction', *J. Hazard. Mater.*, vol. 424, p. 127491, Feb. 2022, doi: 10.1016/j.jhazmat.2021.127491.

[80] S. Sühnholz, A. Gawel, F.-D. Kopinke, and K. Mackenzie, 'Evidence of heterogeneous degradation of PFOA by activated persulfate – FeS as adsorber and activator', *Chem. Eng. J.*, vol. 423, p. 130102, Nov. 2021, doi: 10.1016/j.cej.2021.130102.

[81] S.-R. Yang *et al.*, 'Efficient activation of PAA by FeS for fast removal of pharmaceuticals: The dual role of sulfur species in regulating the reactive oxidized species', *Water Res.*, vol. 217, p. 118402, Jun. 2022, doi: 10.1016/j.watres.2022.118402.

[82] G. Brostigen, A. Kjekshus, E. E. Astrup, V. Nordal, A. A. Lindberg, and J. C. Craig, 'Redetermined Crystal Structure of FeS2 (Pyrite).', *Acta Chem. Scand.*, vol. 23, pp. 2186–2188, 1969, doi: 10.3891/acta.chem.scand.23-2186.

[83] H. Christensen *et al.*, 'Hydrogen Bonds of gamma-FeOOH.', *Acta Chem. Scand.*, vol. 32a, pp. 87–88, 1978, doi: 10.3891/acta.chem.scand.32a-0087.

[84] J. W. Anthony, R. Bideaux, K. Bladh, and M. Nichols, Eds., *Handbook of mineralogy*. Chantilly, VA 20151-1110, USA: Mineralogical Society of America, 1990.

[85] R. A. Berner, 'Iron Sulfides Formed from Aqueous Solution at Low Temperatures and Atmospheric Pressure', *J. Geol.*, vol. 72, no. 3, pp. 293–306, May 1964, doi: 10.1086/626987.

[86] M. Farrand, 'Framboidal sulphides precipitated synthetically', *Miner. Deposita*, vol. 5, no. 3, Aug. 1970, doi: 10.1007/BF00201990.

[87] R. A. Berner, 'Sedimentary pyrite formation', *Am. J. Sci.*, vol. 268, no. 1, pp. 1–23, Jan. 1970, doi: 10.2475/ajs.268.1.1.

[88] R. E. Sweeney and I. R. Kaplan, 'Pyrite Framboid Formation; Laboratory Synthesis and Marine Sediments', *Econ. Geol.*, vol. 68, no. 5, pp. 618–634, Aug. 1973, doi: 10.2113/gsecongeo.68.5.618.

[89] M. A. A. Schoonen and H. L. Barnes, 'Reactions forming pyrite and marcasite from solution: II. Via FeS precursors below 100°C', *Geochim. Cosmochim. Acta*, vol. 55, no. 6, pp. 1505–1514, Jun. 1991, doi: 10.1016/0016-7037(91)90123-M.

[90] D. T. Rickard, 'SULPHIDE FORMATION AT LOW TEMPERA TURES', 1969.

[91] M. A. A. Schoonen and H. L. Barnes, 'Reactions forming pyrite and marcasite from solution: I. Nucleation of FeS2 below 100°C', *Geochim. Cosmochim. Acta*, vol. 55, no. 6, pp. 1495–1504, Jun. 1991, doi: 10.1016/0016-7037(91)90122-L.

[92] J. B. Murowchick and H. L. Barnes, 'Formation of cubic FeS', *Am. Mineral.*, vol. 71, no. 9–10, pp. 1243–1246, Oct. 1986.

[93] 'Netherlands: industry electricity prices 2021', *Statista*. https://www.statista.com/statistics/596254/electricity-industry-price-netherlands/ (accessed May 20, 2023).

APPENDIX

Table of Contents – Appendix

Appendix A Additional Results & Illustrations

A-1 Visualizations Reactor Operation

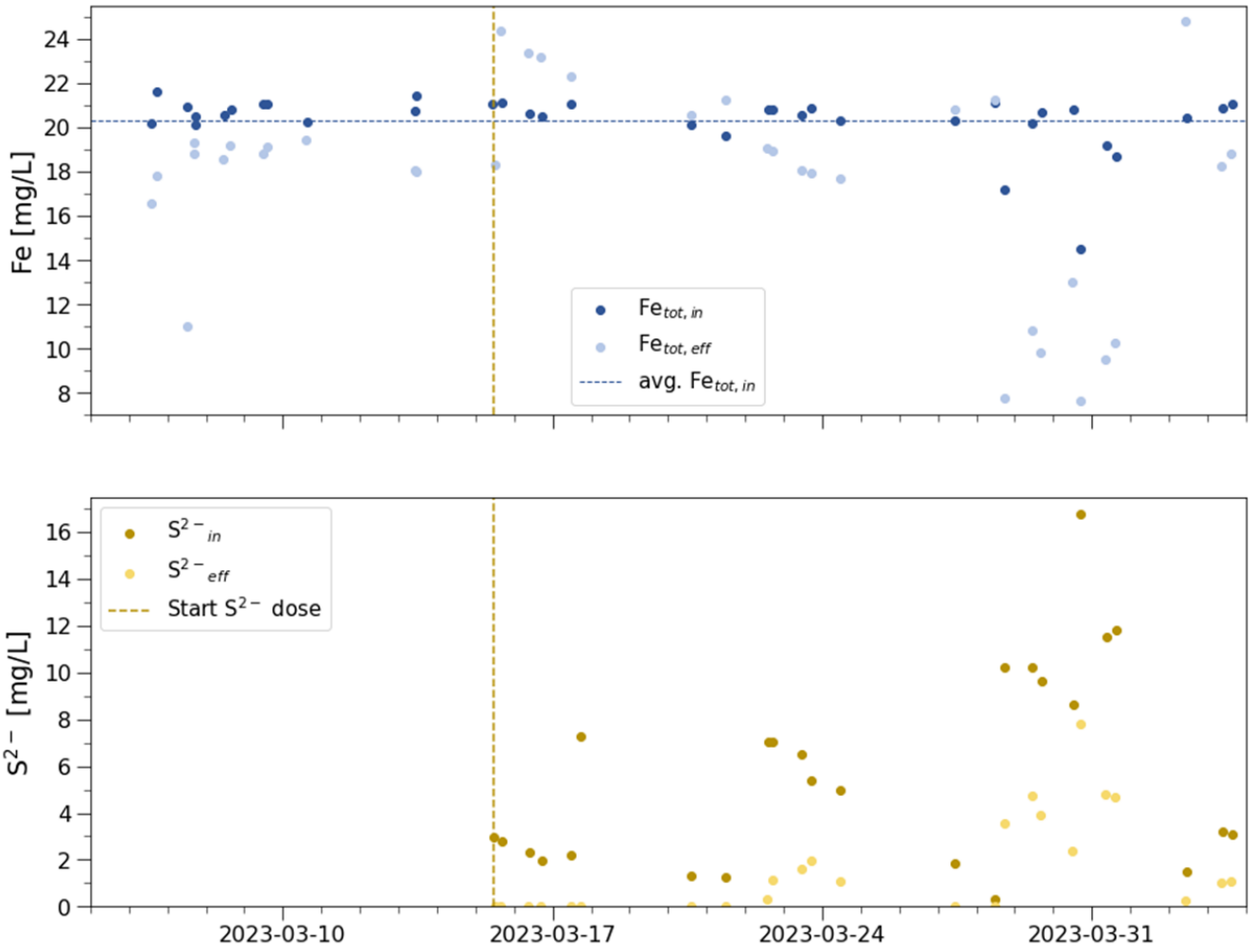

Figure A-1 Complete Timeline of influent and effluent iron and sulfide concentrations of pyrite filled up-flow column reactor.

A-2 XRD Analysis

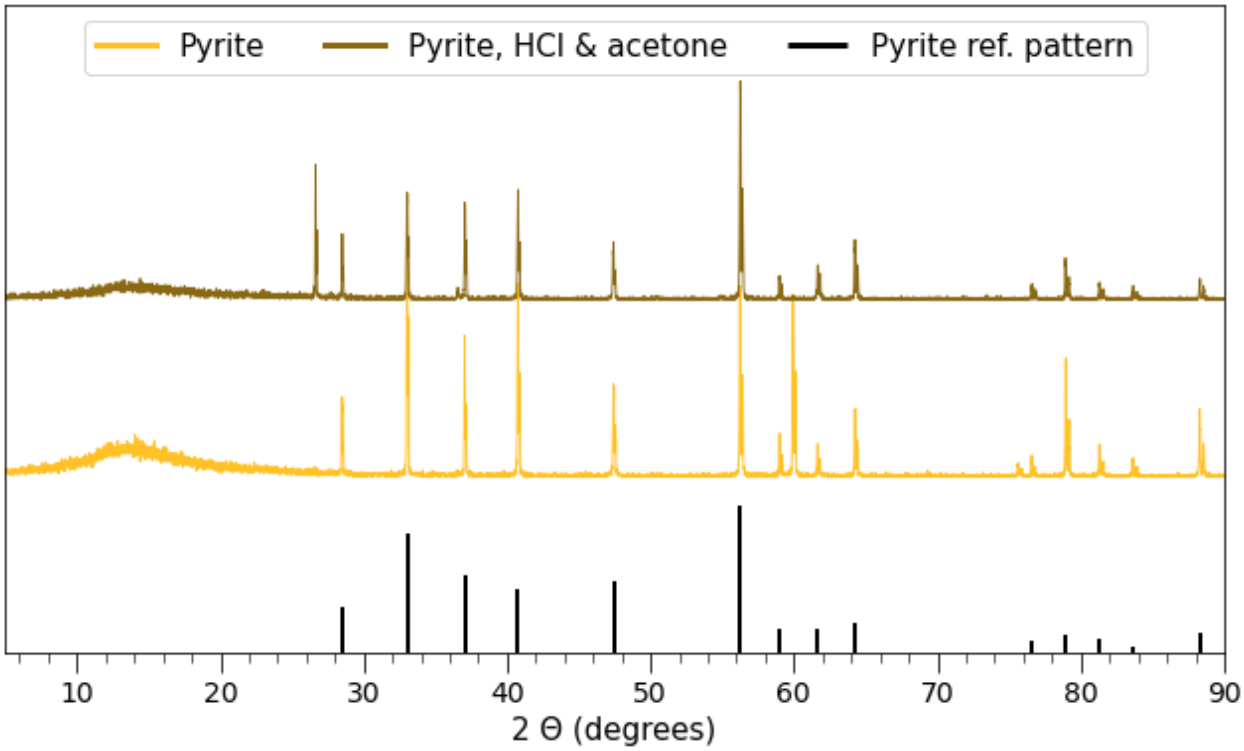

Figure A-2 XRD pattern of pristine grinded pyrite seeding crystals untreated and treated HCl + acetone, respectively. Y-axis shows the relative intensity (arbitrary unit). Ref. pyrite pattern from literature [82].

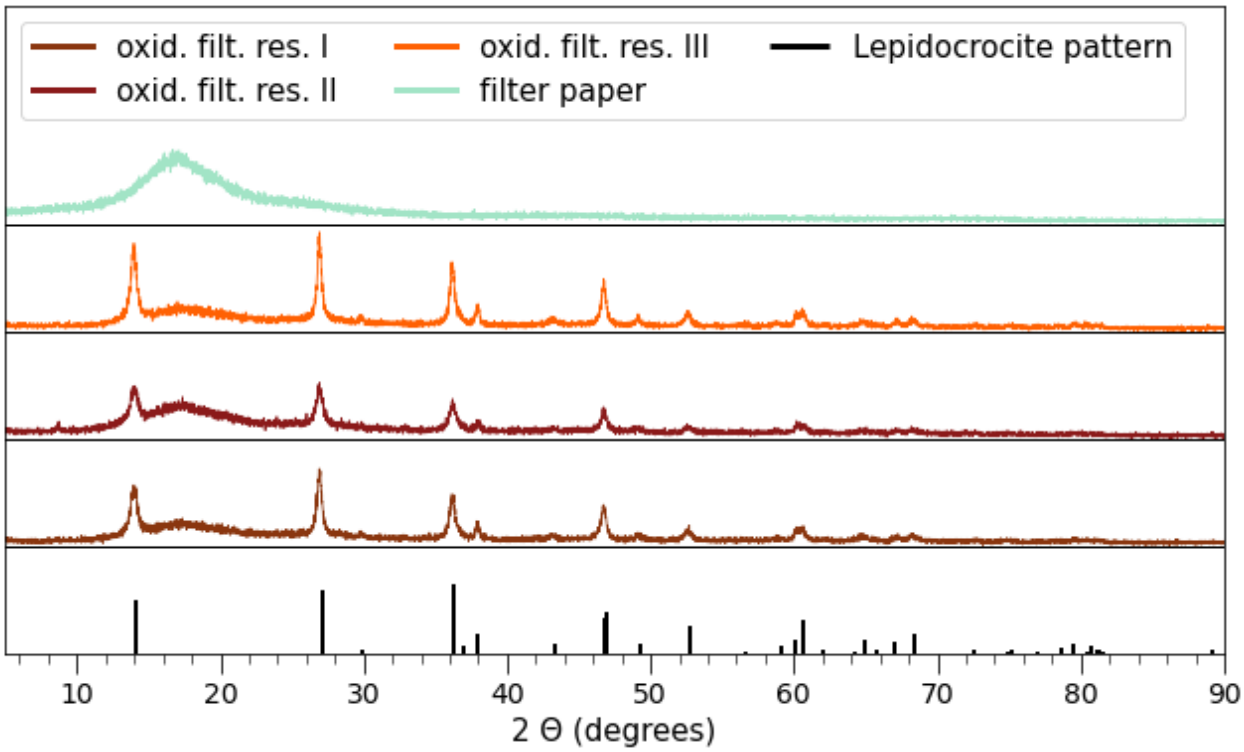

Figure A-3 Three XRD pattern of oxidized effluent solids retained on a 0.1µm filter paper. Y-axis shows the relative intensity (arbitrary unit). Filter paper pattern for reference. Ref. lepidocrocite pattern from literature [83].

A-3 Raman Spectroscopy

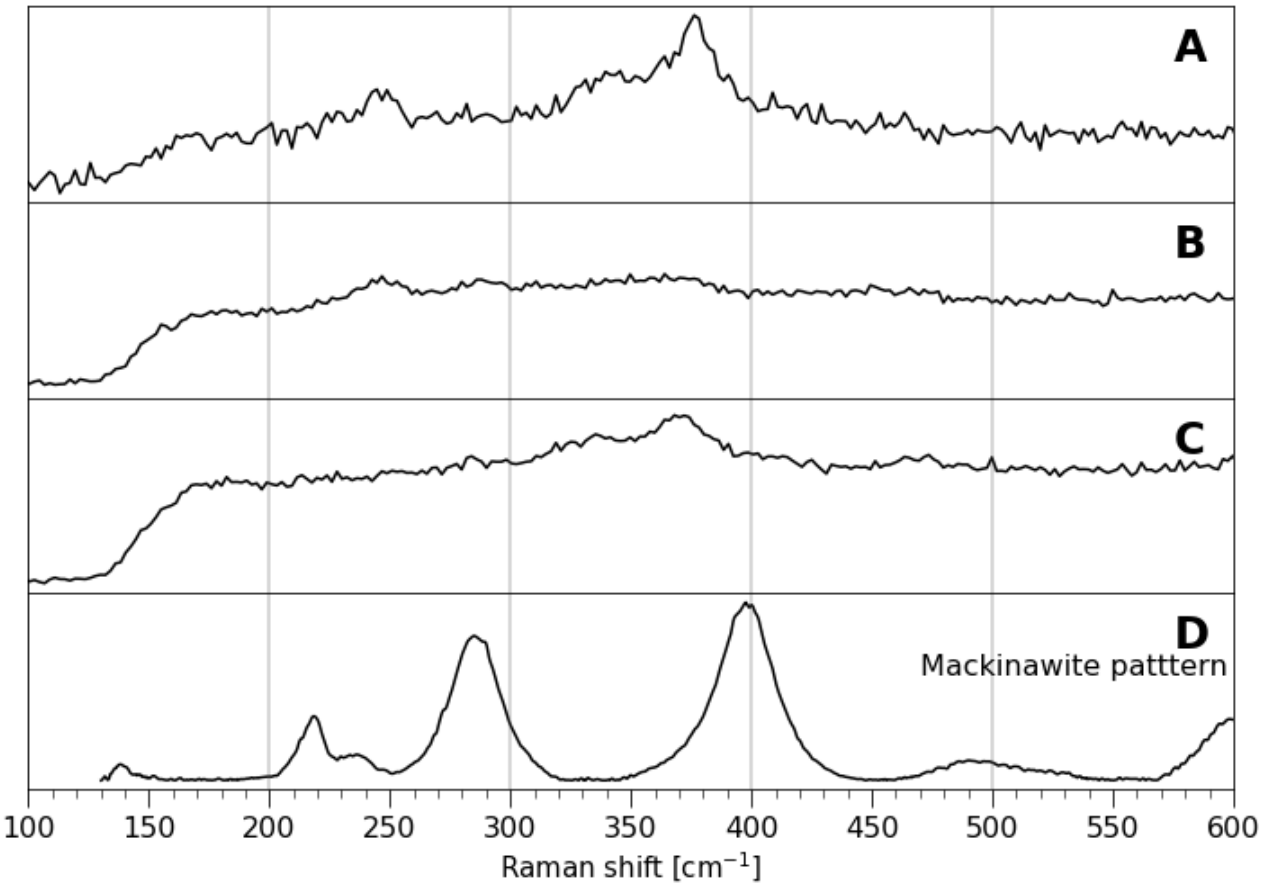

Figure A-4 Raman pattern of effluent suspended solids from dosing ratio Fe:S^{2-}=1:2 (A-C) and Reference pattern for Mackinawite from literature (D) [84]. Y-axis = arbitrary unit.

A-4 Miscellaneous Images of Laboratory Activities

Figure A-5 Effluent sampling via syringe showing clear blackening of the solution. Samples taken during dosing ratio Fe:S^{2-} = 1:2

Figure A-6 Influent sample at dosing ratio of Fe:S^{2-} = 1:2

Figure A-7 Pyrite filled up-flow column reactor before (left) and at the end of experiments (right)

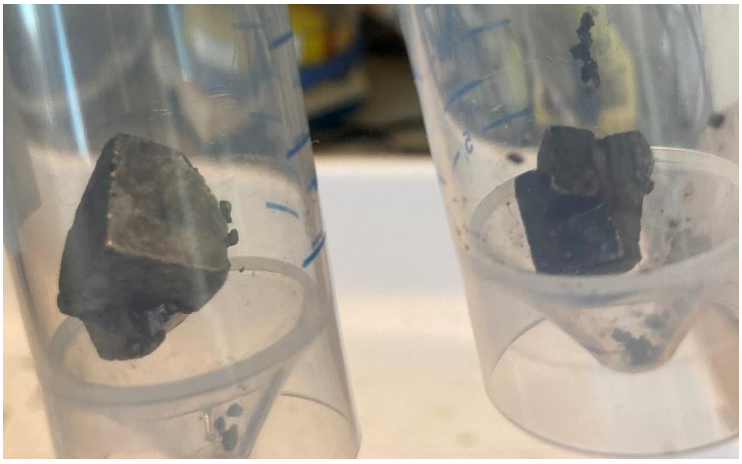

Figure A-8 Cubic Pyrite seeding crystals recovered at the end of the experiments inside the anoxic glovebox. Clear black deposits visible.

A-5 SEM-EDX Specifications of Cubic Pyrite Seeding Crystals after Experiments

A-5-1 Specifications Image A - Figure 3-11

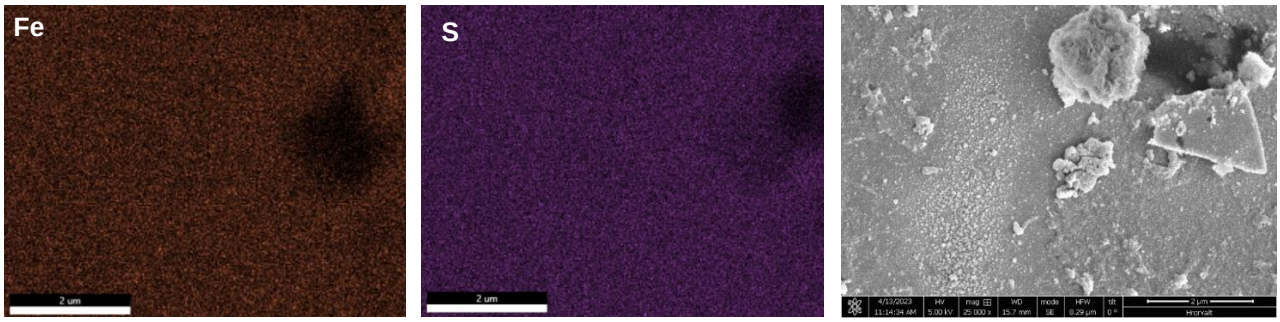

Figure A-9 SEM-EDX of cubic pyrite seeding crystals after experiments. Specifications to Figure 3-11 image A (right). Elemental maps for Fe (left, red) and S (center, purple).

Table A-1 SEM-EDX analysis: Elemental composition. Specifications to Figure 3-11 - A

Element	Weight %	Atomic %	Error %
C	6.2	18.8	11.4
N	0.0	0.1	100.0
O	1.4	3.2	9.4
Fe	20.8	13.6	4.3
Al	0.5	0.7	7.4
Au	18.6	3.5	4.4
S	52.6	60.1	3.1

A-5-2 Specifications Image B - Figure 3-11

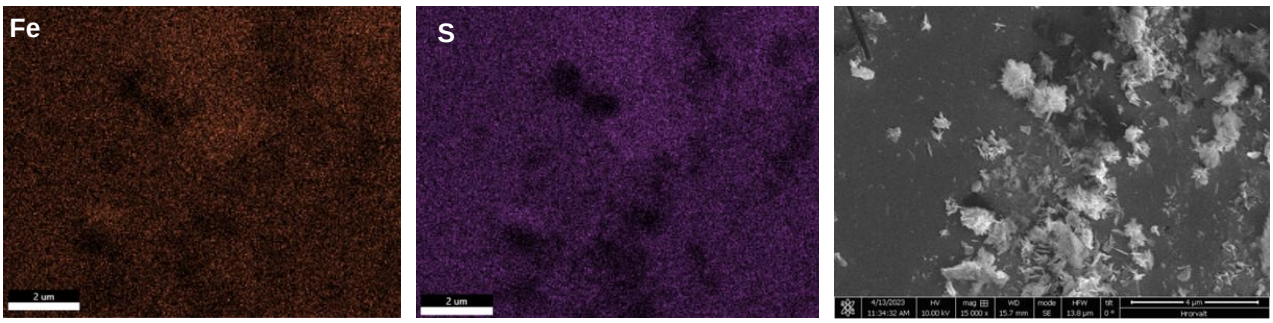

Figure A-10 SEM-EDX of cubic pyrite seeding crystals after experiments. Specifications to Figure 3-11 image B (right). Elemental maps for Fe (left, red) and S (center, purple).

Table A-2 SEM-EDX analysis: Elemental composition. Specifications to Figure 3-11 - B

Element	Weight %	Atomic %	Error %
C	5.1	15.1	12.1
N	0.0	0.0	100.0
O	3.6	8.0	8.8
Fe	23.1	14.8	4.3
Na	0.3	0.5	16.1
Al	0.4	0.5	8.9
Au	15.5	2.8	5.1
S	52.1	58.3	3.1

A-5-3 Specifications Image C - Figure 3-11

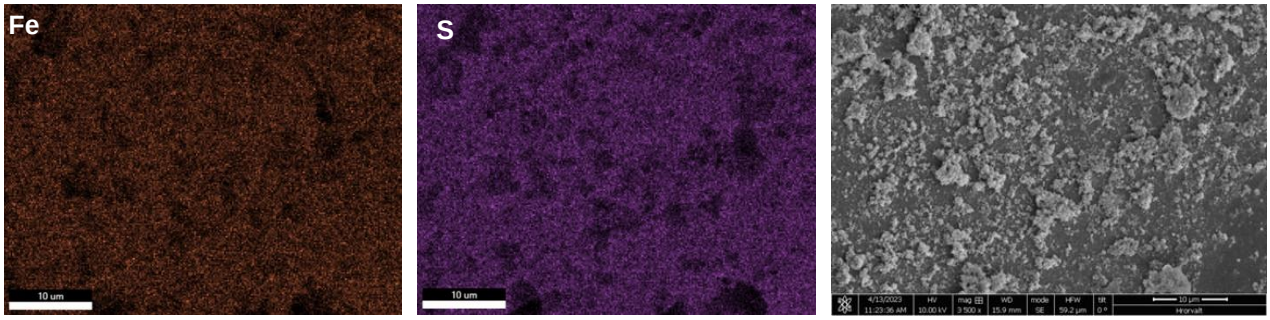

Figure A-11 SEM-EDX of cubic pyrite seeding crystals after experiments. Specifications to Figure 3-11 image A (right). Elemental maps for Fe (red, left) and S (purple, center).

Table A-3 SEM-EDX analysis: Elemental composition. Specifications to Figure 3-11 - C

Element	Weight %	Atomic %	Error %
C	8.5	23.4	11.1
N	0.6	1.4	17.3
O	5.5	11.4	8.1
Fe	19.0	11.2	4.5
Na	0.9	1.2	8.5
Al	0.8	0.9	6.4
Si	0.8	0.9	5.6
Au	18.7	3.1	4.2
S	45.2	46.4	3.2

A-5-4 Specifications Image D - Figure 3-11

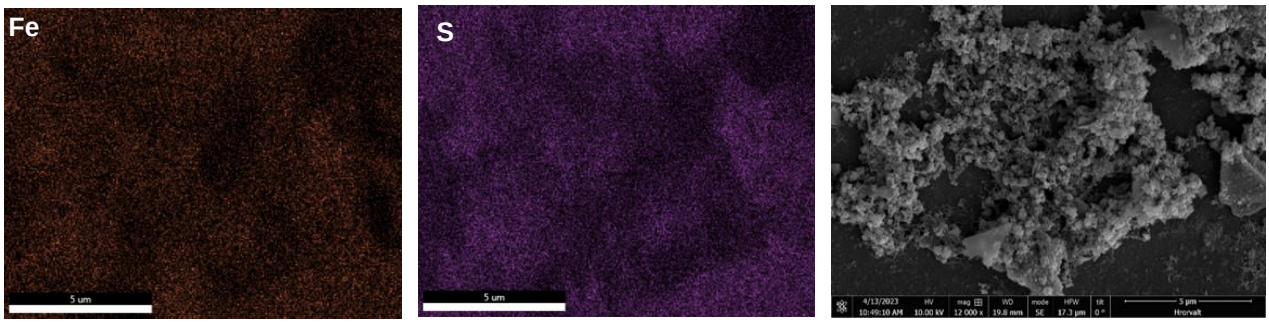

Figure A-12 SEM-EDX of cubic pyrite seeding crystals after experiments. Specifications to Figure 3-11 image D (right). Elemental maps for Fe (red, left) and S (purple, center).

Table A-4 SEM-EDX analysis: Elemental composition. Specifications to Figure 3-11 - D

Element	Weight %	Atomic %	Error %
C	12.1	30.1	11.1
N	0.6	1.3	21.8
O	5.1	9.4	8.3
Fe	14.8	7.9	4.6
Na	3.2	4.1	6.1
Al	0.4	0.4	10.2
Si	0.5	0.5	8.5
Au	16.3	2.5	4.5
S	47.1	43.8	3.1

Appendix B Specifications Experimental Methods

B-1 Test Evaluating Whether FeS_m is Measured by S^{2-} Quantification Method

The goal of this test was to evaluate whether FeS_m bound S^{2-} is included in the S^{2-} quantified by the LCK 653 Hach method. S^{2-} and S^{2-} + Fe^{2+} media samples were taken in triplicate from the reactor inlet sampling port and allowed for 15 minutes to rest in the sampling syringe. FeS_m formation became apparent by blackening of the solution for the S^{2-} + Fe^{2+} media. The S^{2-} media gave a concentration of 4.4 ± 0.0 mg S^{2-}/L. The S^{2-} + Fe^{2+} media resulted in a measured concentration of 4.2 ± 0.3 mg S^{2-}/L. It was therefore concluded that the S^{2-} concentrations indicated by the LCK 653 method includes FeS_m bound sulfide. This matches with observations from another study [76].

B-2 Evaluation S^{2-} Sample Conservation

The goal of this test was to estimate whether zinc acetate and NaOH addition can conserve S^{2-} samples for a week. To investigate this, four sulfide samples were taken at different time points. A fraction of each sample was analyzed immediately, the remainder was conserved with zinc acetate and NaOH for measurements after eight days respectively. The immediately measured and conserved samples yielded in a concentration of 6.9 ± 1.1 mg S^{2-}/L and 7.2 ± 1.2 mg S^{2-}/L, respectively. The conservation method was therefore seen effective. This aligns with findings from another study [45].

B-3 Protocol: Sampling Procedure for Hach Kits Analysis

This section shows the key notes of the sequence of steps utilized for sampling the reactor.

Important note:

- sample fast as iron oxidizes and sulfide escapes
- flush syringes and filters with N_2 before sampling
- sample effluent first

1. fill DI water according to dilution rate in Hach vial using a pipette
2. Sampling of reactor
    a. influent
        i. close valve in front of reactor
        ii. open sample valve
    b. effluent
        i. close valve in front of EC flow cell
        ii. open sample valve
3. drain media for 2 minutes
4. connect 10mL syringe to collect sample
5. fill sample gently in 10mL beaker
6. mix gently with pipette tip
7. take desired volume from 10mL beaker
8. Follow Hach Method for further steps

Appendix C Specifications on Devices, Chemicals and Analytical Procedures

Table C-1 Overview of used chemicals and respective suppliers

Chemical	Formula	Supplier
Sodium sulfide nonahydrate, 98%, ACS	$Na_2S \cdot 9H_2O$	Merck Sigma, Germany
Sodium sulfite 98+%, A.C.S	Na_2SO_3	Merck Sigma, Germany
Mohr's salt ACS	$(NH_4)_2Fe(SO_4)_2 \cdot 6H_2O$	Merck Sigma, Germany
Sodium hydroxide ACS	NaOH	Merck Sigma, Germany
Hydrochloric acid ACS	HCl	Honeywell, US
Sodium chloride ACS	NaCl	Merck Sigma, Germany
Sodium bicarbonate ACS	$NaHCO_3$	Merck Sigma, Germany
Zinc acetate ACS	$Zn(CH_3CO_2)_2 \cdot 2H_2O$	Merck Sigma, Germany

Table C-2 Overview of used devices and respective manufacturers

Device	Manufacturer
XRD - D8 Advance Eco	Bruker Corporation, USA
pH Sensor - InPro 3250i/SG/225 – sulfide resistant	Mettler Toledo, Switzerland
IDS pH-Electrode SenTix® 940	Xylem Analytics, USA
EC-Sensor - TetraCon® 925	Xylem Analytics, USA
Optical IDS dissolved oxygen sensor FDO® 925	Xylem Analytics, USA
DR3900 Laboratory VIS Spectrophotometer	Hach Lange GmbH, Germany
NovaNano SEM	FEI, USA
Raman Spectroscopy - Renishaw Invia Reflex	Renishaw, UK
Peristaltic pump,120 U Multi 3630 IDS	Watson Marlow, UK
H_2S sensor, BW Clip Real Time	Honeywell, US

Appendix D Supporting Information on Iron Sulfide Chemistry

D-1 Overview of Iron Sulfides

Table D-1 Solid Phases in the Fe-S System. Table from [20].

Material	Composition	Properties
Mackinawite	FeS_m	metastable material that is the major constituent of the FeS precipitated from aqueous solutions
Cubic FeS	FeS_c	highly unstable phase formed before FeSm
Troilite	FeS_t	stoichiometric end member of the $Fe_{1-x}S$ group
Pyrrhotite	$Fe_{1-x}S$	nonstoichiometric stable group where x > 0.2; monoclinic form is approximately Fe_7S_8; hexagonal form is approximately $Fe_{10}S_{11}$
Smythite	Fe_9S_{11s}	metastable phase related to the $Fe_{1-x}S$ group
Greigite	Fe_3S_4	metastable Fe(II)-Fe(III) sulfide; the thiospinel of iron
Pyrite	FeS_{2p}	stable iron(II) disulfide known as “fool’s gold”
Marcasite	FeS_{2m}	metastable iron(II) disulfide

D-2 Overview of Experimental Aqueous Pyrite Formation Recipes from Fe(II) at Ambient Temperatures and Formation Rates

Table D-2 Reported Recipes for experimental pyrite formation at low temperatures from Fe(II). Modified from [20], [21] and supplemented

Fe reactant	S reactant	pH	T [°C]	Ref.
$FeSO_4$, $(NH_4)_2Fe(SO_4)_2{\cdot}6H_2O$	H_2S	3-5	20-95	[85]
$FeSO_4$,	H_2S	7-8	25	[86]
$FeSO_4$, $(NH_4)_2Fe(SO_4)_2{\cdot}6H_2O$	$H_2S + S_8$	6.9-7.9	65	[87]
$FeCl_2$	$H_2S + S_8$	-	25-60	[88]
$(NH_4)_2Fe(SO_4)_2{\cdot}6H_2O$, $FeCl_2$	$NaHS + S_8$	65	1.5-8.8	[89]
$FeSO_4$, $FeCO_3$	Na_2S_n[g]	25	4.4-9.5	[90]
$FeSO_4$, $(NH_4)_2Fe(SO_4)_2{\cdot}6H_2O$, $FeCO_3$, $FeCl_2$	$NaHS + Na_2S_4$	7.3-7.6	25	[91]
$FeCl_2$, $FeSO_4$, $(NH_4)_2Fe(SO_4)_2{\cdot}6H_2O$	Na_2S_2, Na_2S_4, Na_2S_5	5.5-8	25, 100	[53]
Fe(II)[3]	$H_2S + Na_2S_2O_3$	3.4-6.9	75	[92]
$(NH_4)_2Fe(SO_4)_2{\cdot}6H_2O$	NaHS	6.5	25	[41]
$(NH_4)_2Fe(SO_4)_2{\cdot}6H_2O$	Na_2S	6-6.5	20-40	[43]
$(NH_4)_2Fe(SO_4)_2{\cdot}6H_2O$	Na_2S	6-6.1	40	[58]
$(NH_4)_2Fe(SO_4)_2{\cdot}6H_2O$	Na_2S	6	40-100	[38]

[3] Not specified

The rate equation for pyrite formation is shown in equation (6) [40].

$$\frac{dFeS_{2,p}}{dt} = k_p\ (FeS)\ (c\ H_2S_{(aq)}) \tag{6}$$

With k_p= second order rate constant for pyrite formation (1.03 x 10^{-4} – 3.2 x 10^{-3} L mol^{-1} s^{-1}, between 25°C and 125°C). FeS includes the precipitated form, since the dissolution kinetics of FeS are usually faster than the formation rates of pyrite [40].

Rate equation for mackinawite formation is shown in equation (7) [21].

$$\frac{dFeS_m}{dt} = k_m\ (Fe^{2+})\ (c\ H_2S_{(aq)}) \tag{7}$$

With k_m = second order rate constant for mackinawite formation (7 ± 1 L mol^{-1} s^{-1}).

Looking at the formation rate constant of pyrite and mackinawite, it can be seen that the formation of mackinawite is three magnitudes faster than the formation of pyrite. However, mackinawite is unstable with respect to pyrite .The equilibrium concentration of mackinawite to its dissolved ions is sufficient to reach a supersaturation allowing for pyrite formation. Therefore, in natural systems mackinawite usually dissolves to ultimately form the stable phase pyrite.

D-3 Eh-pH Stability Diagrams for Iron and Sulfur Systems

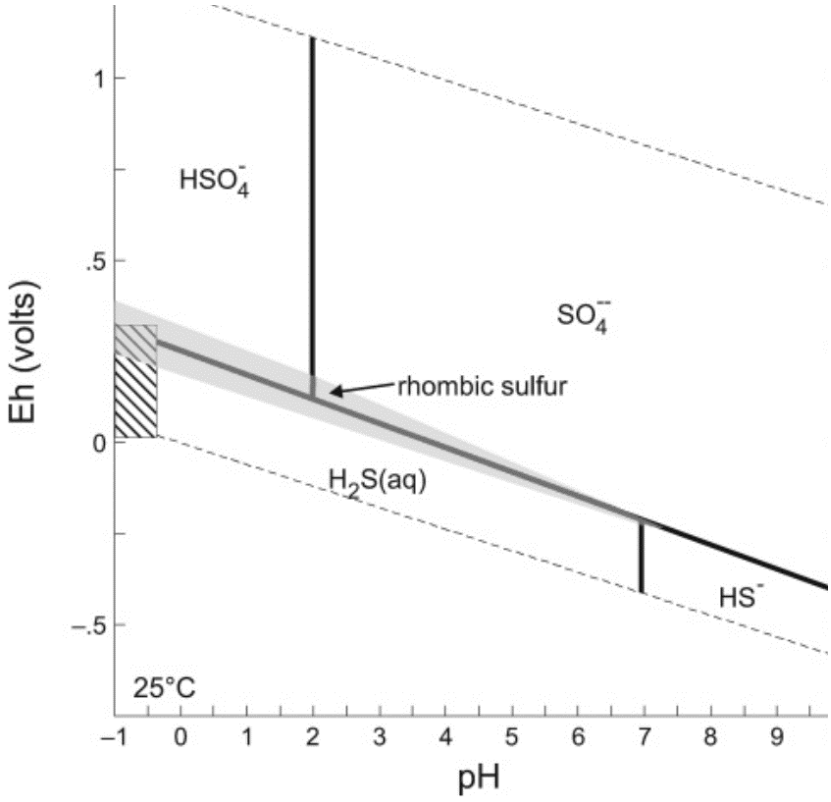

Figure D-1 "Conventional pH-Eh equilibrium diagram for sulfur species at 25 °C and 1 atm pressure" from [20]

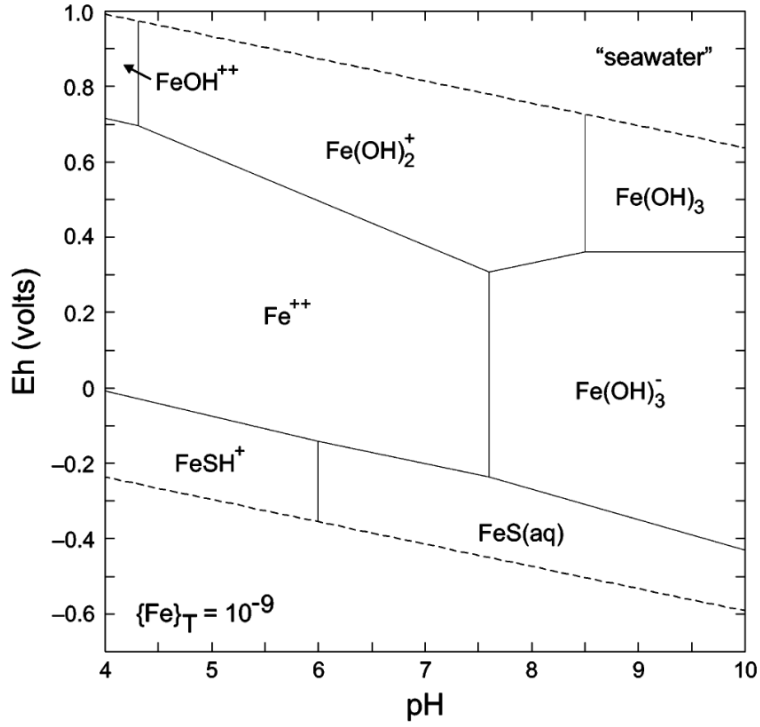

Figure D-2 "pH-Eh diagram of the relative stability of the inorganic dissolved Fe species in an inorganic solution with an average seawater composition and a total dissolved Fe(II) activity of 10^{-9}." From [20]

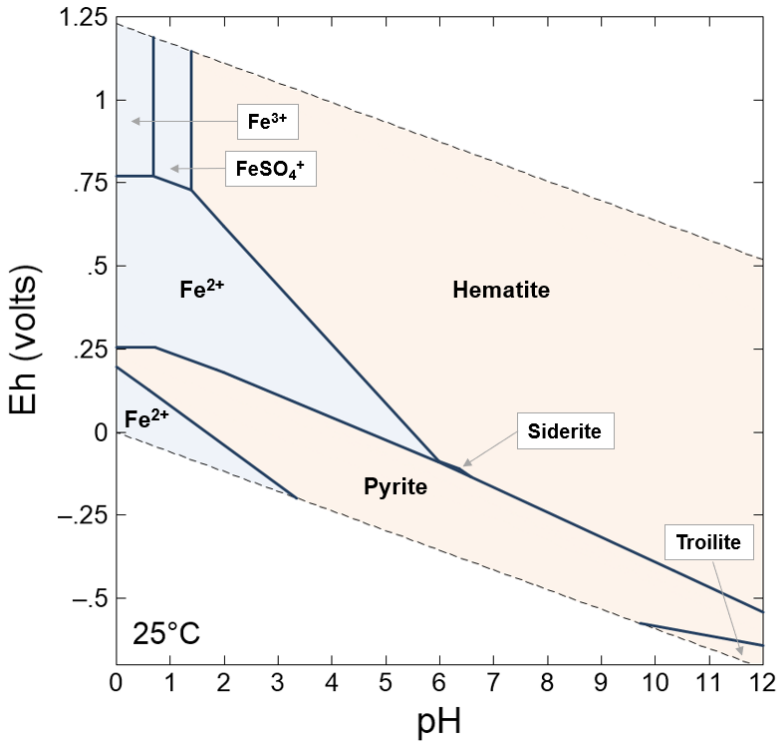

Figure D-3 Eh-pH diagram for stable species of the "Dose Fe:S^{2-} = 1:1" media according to Table 2-1 (25°C, 1.013 bars, activity coefficients =1); blue areas mark dissolved species, red undissolved minerals; made with GWB

Appendix E Phreeqc Models

E-1 Effect of Sulfide Dose on Redox Potential

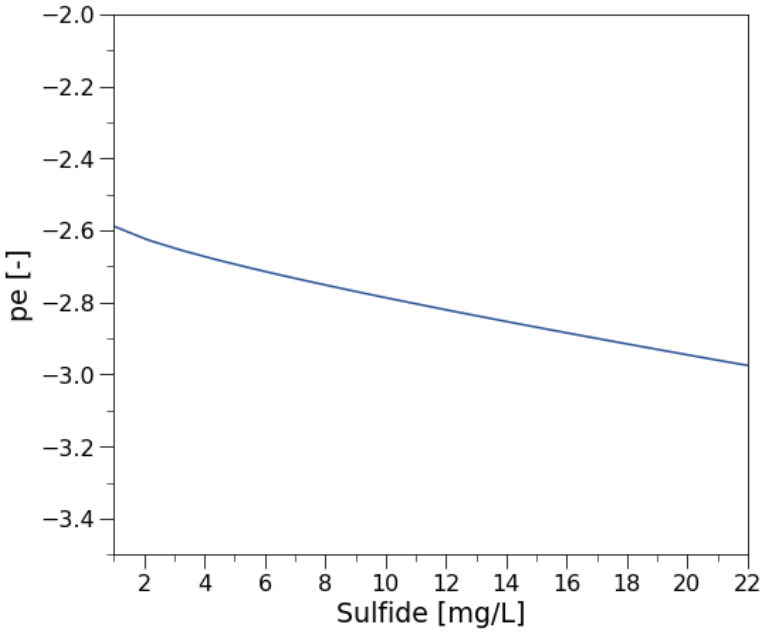

Figure E-1 Effect of sulfide dose on redox potential

```
SOLUTION    1 TAPW
temp    20
pH      6.1
pe      -3.4
-units  mg/l
Alkalinity      171 as HCO3
Na      78.8
END

USE solution 1
REACTION
Na2S
7.2e-4 moles in 20 steps  # equals ca. 23 mg S2-/L
End
```

Phreeqc source code: Effect of Sulfide concentration on redox potential

E-2 Mackinawite Equilibrium Solubility at pH=6.1

The equilibrium concentrations at a pH of 6.1 equal 0.3 mg S^{2-}/L and 1.9mg Fe^{2+}/L.

```
SOLUTION    1 TAPW
temp    12.7
pH      6.1
pe      -3.4
-units  mg/l
Alkalinity      171 as HCO3
```

```
Cl      50
Ca      49.7
Mg      7.0
Na      41.6
O(0)    0
N(5)    2.4
S(-2)   11.5
Fe(+2) 20

END

PHASES
      Fix_H+
      H+ = H+
      log_k  0.0
END

USE solution 1
EQUILIBRIUM_PHASES
Mackinawite     0 0
fix_H+ -6.1   HCl    1.0
End
```

Phreeqc source code: Mackinawite equilibrium solubility at pH = 6.1 for typical GW-matrix

E-3 SI of Pyrite at Fe:S^{2-} = 1:2 Dosing Ratio & pH 6

The calculated SI of pyrite equals 17.5.

```
SOLUTION     1 EXP_MEDIA
temp    20
pH      6
pe      0
-units   mg/l
Alkalinity        171 as HCO3
Na      126
Cl      102
O(0)    0
S(+6)   69
# sulfite cannot be added
Amm   13 as NH4
S(-2)   12
Fe(+2) 20

END
```

Phreeqc source code: SI of Pyrite at Fe:S^{2-} = 1:2 Dosing Ratio & pH 6

Appendix F Cost Calculation Electrochemical Sulfide Dose

The costs of sulfate reduction for sulfide dose were estimated by applying Faraday's Law using the following equation:

$$p_{m^3} = C_{S^{2-}}\ z_{S^{2-}}\ V\ F\ \ s_f\ p_{elec.}\ \eta\ 2.78 * 10^{-7}\ \frac{kWh}{J} \quad (8)$$

With:

p_{m^3} = price per m³ [€/m³]
V = voltage (1.8V) [V] [33]
$C_{S^{2-}}$ = concentration of dosed sulfide [mol S^{2-}/L]
$z_{S^{2-}}$ = number of transferred electrons for full reduction of sulfate to sulfide [8 mol e^-/ mol S^{2-}]
F = Faraday's constant (96485 C mol^{-1})
s_f = 1.3 [-]
$p_{elec.}$ = 0.11 [€/kWh] [93]
η = efficiency (0.8) [-] [33]

The mM concentration of dosed sulfide equaled the mM iron concentration for the mackinawite calculation. For the pyrite calculation it was double the concentration. This is according to the molar Fe:S ratios of the respective molecules.


TU Delft